Available online at www.sciencedirect.com

ScienceDirect

Journal of Magnesium and Alloys 11 (2023) 1769–1790

www.elsevier.com/locate/jma

Full Length Article

Simple shear extrusion versus equal channel angular pressing: A comparative study on the microstructure and mechanical properties of an Mg alloy

A. Rezaei[a], R. Mahmudi[a,*], C. Cayron[b], R.E. Logé[b]

[a] School of Metallurgical and Materials Engineering, College of Engineering, University of Tehran, North Kargar Street, Tehran 14395-515, Iran
[b] Laboratory of Thermomechanical Metallurgy - PX Group Chair, Ecole Polytechnique Fédérale de Lausanne (EPFL), Neuchâtel CH-2002, Switzerland

Received 4 November 2022; received in revised form 3 May 2023; accepted 7 May 2023
Available online 8 June 2023

Abstract

Two severe plastic deformation (SPD) techniques of simple shear extrusion (SSE) and equal channel angular pressing (ECAP) were employed to process an extruded Mg−6Gd−3Y−1.5Ag (wt%) alloy at 553 K for 1, 2, 4 and 6 passes. The microstructural evolutions were studied by electron back scattered diffraction (EBSD) analysis and transmission electron microscopy (TEM). The initial grain size of 7.5 μm in the extruded alloy was reduced to about 1.3 μm after 6 SPD passes. Discontinuous dynamic recrystallization was suggested to be operative in both SSE and ECAP, with also a potential contribution of continuous dynamic recrystallization at the early stages of deformation. The difference in the shear strain paths of the two SPD techniques caused different progression rate of dynamic recrystallization (DRX), so that the alloys processed by ECAP exhibited higher fractions of recrystallization and high angle grain boundaries (HAGBs). It was revealed that crystallographic texture was also significantly influenced by the difference in the strain paths of the two SPD methods, where dissimilar basal plane texture components were obtained. The compression tests, performed along extrusion direction (ED), indicated that the compressive yield stress (CYS) and ultimate compressive strength (UCS) of the alloys after both SEE and ECAP augmented continuously by increasing the number of passes. ECAP-processed alloys had lower values of CYS and UCS compared to their counterparts processed by SSE. This difference in the mechanical responses was attributed to the different configurations of basal planes with respect to the loading direction (ED) of each SPD technique.

Keywords: Mg-Gd-Y alloys; Severe plastic deformation; Simple shear extrusion; Equal channel angular pressing; Dynamic recrystallization; Mechanical properties.

1. Introduction

During the recent decades, the anthropogenic emissions of the greenhouse gasses have been recognized as the prominent contributor to global warming, a detrimental worldwide-class phenomenon which substantially stems from the pollution generated by the ceaseless-flourishing transportation industries. Thus, reducing the consumption of the fossil fuels through lowering the weight of the vehicles would be a promising approach to address such adversity. Adopting Mg alloys could serve the aforementioned weight-saving purpose, as they are recognized to be the lightest structural metals [1,2]. However, this well-known advantage of Mg alloys has come with a price that limits their industrial applications. Since magnesium has only two independent slip systems [3,4], it suffers from poor formability at room temperature that makes their deformation challenging [5]. More importantly, suitable Mg alloys with high strength are demanded for structural components. This has raised a renewed enthusiasm in the literature to develop and process different Mg alloys with the required structural qualifications. Even

* Corresponding author.
E-mail address: mahmudi@ut.ac.ir (R. Mahmudi).

https://doi.org/10.1016/j.jma.2023.05.006

though raising the working temperature improves the formability of Mg alloys during conventional forming processes of hot extrusion and hot rolling, through activating the non-basal slip systems [6], the occurrence of inevitable dynamic grain growth during hot working leads to the deterioration of post-deformation mechanical properties.

Different severe plastic deformation (SPD) techniques such as equal channel angular pressing (ECAP), accumulative roll bonding (ARB), friction stir processing (FSP), high pressure torsion (HPT), cyclic extrusion and compression (CEC), multi directional forging (MDF), and constrained groove pressing (CGP) have all been known as effective processing methods to improve the mechanical properties of Mg alloys by causing remarkable grain refinement [7–11] and reducing the anisotropy [12,13] through modifying the crystallographic texture. Among these SPD techniques, ECAP has been found to be one of the most efficient ones in refining the microstructure, and also recognized as an affordable processing tool due to its simplicity of design and ease of equipment fabrication [14].

After 8 ECAP passes of a cast Mg−10.6Gd−2Ag alloy at 623 K, conspicuous rise in the respective tensile yield and ultimate strength values from 100 to 210 MPa for the as-cast alloy to 317 and 417 MPa for the ECAPed one was reported [15]. This significant improvement in the strength was ascribed to the decrease in the grain size from 150 μm in the as-cast state to the fine dynamically recrystallized grains within the range of 1 to 2 μm, and also the formation of precipitates after being processed by ECAP. Similar enhancement in mechanical response was reported [16] for a homogenized Mg−13Gd−4Y−2Zn−0.6Zr cast alloy after 3 passes of ECAP at 723 K, wherein the grain size reduced from 105 μm in the homogenized state to 10.9 μm after ECAP. This augmentation in mechanical behavior was attributed to the concurrent effects of the increase in fraction of fine dynamically recrystallized (DRXed) grains and the fragmentation of the intragranular long period-stacking order (LPSO) phases after processing through ECAP. Although most of the works in the literature report the refined grain sizes greater than 1 μm for Mg alloys after being processed by ECAP [17–19], achieving much finer microstructures in the ultra-fine grained (UFG) or submicron category would be practical through tailoring the processing parameters such as lowering of the processing temperature [20,21]

Developing new SPD techniques or reconsidering the tools design of the existing ones would always be demanding to optimize the processing conditions for the hard-to-deform metals with HCP structure such as Mg alloys. Accordingly, Pardis and Ebrahimi [22] came up with the idea of gradually imposing shear strain on the workpiece as the specimen advances through a forward extrusion channel. This newly developed SPD technique was named simple shear extrusion (SSE). The extrusion die in the SSE method is comprised of a deformation channel with a specific curved-shape, the inner periphery of which causes the workpiece to experience a strain in the simple shear deformation mode in a reciprocal manner. Later, Bayat Tork et al. [23] investigated the feasibility of processing pure Mg at room temperature via two methods of SSE and ECAP. Their results showed that pure Mg specimens were successfully processed by SSE technique, whereas the ones processed through ECAP were fractured and segmented, showing a characteristic shear pattern appearance due to the strain localization in the shear plane of the process. The intrinsic low strain rate of SSE makes it an advantageous method over ECAP in order to process the hard-to-deform alloys even at temperatures lower-than-expected.

The Mg-6Gd-3Y-1.5Ag (wt%) alloy was chosen in this study to serve as a high-strength model material to investigate the differences in microstructural, textural and mechanical features, caused by the two methods of SSE and ECAP. The similarities in terms of identical shear deformation modes and also similar strain levels per each pass are the reasons that make the comparison between SSE and ECAP interesting and noteworthy. Despite these similarities, there are substantial differences in the geometrical features and tool design that leads to emerging a totally different strain path in each of these techniques. In some certain circumstances, such as processing of the hard-to-deform materials, the SSE technique could be a more suitable candidate than ECAP, as the shear strain is imposed on the workpiece gradually leading to reduced chance of fragmentation and failure. However, no previous report has been published on industrializing SSE method as its tool design and fabrication is more complicated than ECAP. Hitherto, no systemic study has been reported on the role of different strain paths in SSE and ECAP on the microstructural, textural and mechanical features of an Mg alloy. Thus, the aim of this study was set to investigate the microstructural characteristics and crystallographic texture of the extruded Mg−Gd−Y−Ag alloy, processed by both SSE and ECAP under identical processing conditions and relating these observations to the mechanical properties.

2. Experimental procedure

A magnesium alloy with the nominal composition of Mg−6wt% Gd−3wt% Y−1.5wt% Ag was prepared by the melting of high purity (99.9 wt%) Mg ingot, silver pellets, and two master alloys of Mg−30Gd and Mg−30Y. Melting was performed in an electrical resistance furnace at temperature of 1053 K under a covering flux to prevent oxidation. The melt was kept in the furnace for 20 min before being poured into a steel mold which was preheated to 453 K. The as-cast billet was homogenized at 773 K for 10 h and then cooled to room temperature in the air. Afterwards, the homogenized billet of 40 mm diameter was hot extruded at 673 K at a cross-head speed of 5 mm min^{-1} with an extrusion ratio of 11.4 to produce bars with a cross section of 11 × 11 mm.

Specimens with a length of 30 mm were cut from the extruded bars and their cross sections were reduced to 10 × 10 mm using grinding in order to be fed into the SSE die channel. The SSE process was performed at the temperature of 553 K and a ram speed of 0.1 mm s^{-1} for 1, 2, 4 and 6 passes using route “C” [24], in which the specimen is rotated 90° clockwise around the extrusion direction (ED)

between consecutive passes. To reduce friction, all the SSE specimens were wrapped in poly tetra fluoro ethylene (PTFE) tapes before starting each new pass. The SSE method employed in this study consists of a forward extrusion die having a parabolic profile path along the inner periphery of the deformation channel with an effective length of 60 mm and a maximal distortion angle of $\alpha_{max} = 45°$ in the middle of the channel of the SSE die. The maximum distortion angle of α_{max} equal to 45° leads to an equivalent mean strain of 1.15 for each pass of SSE. The schematic presentation of a deformed specimen in the deformation channel of SSE process is displayed in Fig. 1a. For more detailed information on the characteristics of the SSE process used in the current study, the readers are referred to our previous work [25].

The dimensions of the ECAP specimens were 60 × 10 × 10 mm and the temperature and ram speed were chosen exactly identical to those for the SSE method, i.e., 553 K and 0.1 mm s^{-1}, respectively. The ECAP specimens were also processed for 1, 2, 4 and 6 passes using route B_C, in which the workpiece is rotated 90° around ED. The ECAP die had two intersecting channels with a die angle of $\phi = 90°$ and an outer arc of curvature of $\psi = 20°$ The mean strain for each pass of ECAP would be equal to 1.02 that is slightly smaller than that for SSE method. Fig. 1b demonstrates the schematic illustration of the deforming specimen during ECAP process. Table 1 summarizes information on the processing conditions of all specimens, and also the nomenclatures designated to different specimens either processed by SSE or ECAP.

Electron back scattered diffraction (EBSD) analysis was performed on a plane normal to ED for all conditions. The sample preparation details for EBSD studies are given elsewhere [25]. The EBSD data were processed by MTEX [26] that is operative on the basis of MATLAB computer software. For all the EBSD results, the boundaries with misorientation angles within the range of 2° and 15° were considered as low angle grain boundaries (LAGBs); and those with misorientation angles greater than 15° were taken as high angle grain boundaries (HAGBs). The recrystallization fractions were calculated according to the grain orientation spread (GOS) values of the grains; the grains with GOS values lower than a critical limit of 2° were defined as recrystallized, while the ones with the greater GOS values were labeled as deformed. The density of geometrically necessary dislocations (GNDs) obtained from the EBSD data through MTEX software was based on calculating lattice curvature tensor for each pixel and correlating it to dislocation density tensor, while holding a minimum stored dislocation energy. A more detailed investigation on calculating GND density from the EBSD data is given in the work of Pantleon [27]. Scanning electron microscopy (SEM) was also utilized to investigate the initial microstructure of the extruded alloy. The sample preparation procedure for SEM studies were identical to those for EBSD. Transmission electron microscopy (TEM), using an FEI-Tecnai-Osiris instrument equipped with four Super-XSDD EDS detectors, was carried out to study the microstructural features of the alloys after being processed by

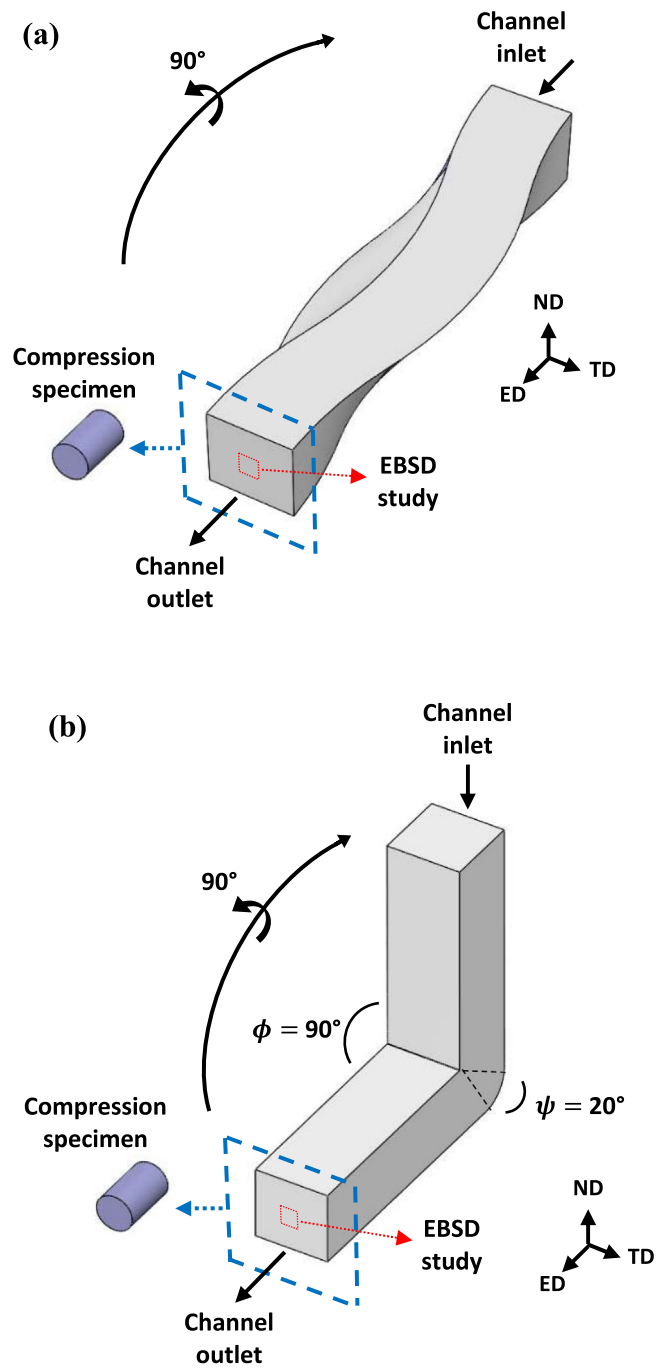

Fig. 1. Schematic illustrations of the way in which the extruded alloys are deformed in the processing channel of SSE (a) and ECAP (b) techniques, and how the compression test specimens are cut perpendicular to the ED direction.

6 passes of both SSE and ECAP at higher magnifications in a plane normal to ED. The procedure for the preparation of the TEM foils can be found in our previous study [28].

Mechanical properties of the as-extruded and severely deformed conditions were assessed through uniaxial compression testing with the loading direction along ED. The cylindrical compression specimens with the respective diameters and heights of 5 and 8 mm were cut via electro-discharge

Table 1
The nomenclature designated to the Mg−6Gd−3Y−1.5Ag alloy in this study according to their processing conditions.

Specimen designation	Processing technique	Number of passes	Mean strain	Route
SSE-1P	SSE	1	1.15	–
ECAP-1P	ECAP	1	1.02	–
SSE-2P	SSE	2	2.3	C
ECAP-2P	ECAP	2	2.04	B_C
SSE-4P	SSE	4	4.6	C
ECAP-4P	ECAP	4	4.08	B_C
SSE-6P	SSE	6	6.9	C
ECAP-6P	ECAP	6	6.12	B_C

machining (EDM) from the as-extruded and processed materials. The way in which the compression specimens were prepared with their longitudinal axis parallel to ED for both SSE and ECAP is illustrated in Fig. 1. The compression tests were carried out using a universal screw driven testing machine under an initial strain rate of 1×10^{-4} s^{-1}, where the ends of the specimens were lubricated to reduce the friction and the corresponding barreling effect.

3. Results

3.1. Initial microstructure of the extruded alloy

Fig. 2a and b displays the SEM micrographs of the extruded alloy at two different magnifications in a plane normal to ED. As can be observed in Fig. 2b, there are two sets of second phase particles distributed mainly at the grain boundaries: (1) some particles with a cuboid shape that are larger in size marked by a red arrow as “A”, and (2) another group of particles with irregular shape and smaller size marked as “B” (Fig. 2b). The EDS analysis showed that the cuboid particles are Mg_2 (Gd,Y) (Fig. 2c). The finer particles with irregular shape, however, have a stoichiometry close to the $Mg_{16}Gd_2YAg$ composition (Fig. 2c) that can be categorized as Mg_5Gd-type intermetallic phase. In our previous work [29], it was shown via XRD analysis that the large cuboid shape particles formed in an Ag-free extruded Mg−6Gd−3Y alloy have characteristic picks corresponding to the FCC Mg_2Gd-type phase. In the case of the Ag-containing alloy, smaller particles had the composition of $Mg_{16}Gd_2YAg$. Such a phase was already observed after addition of 1 wt% Ag to an extruded Mg−6Gd−3Y alloy [29]. Similarly, Movahedi-Rad and Mahmudi [30] observed Ag-containing second phase particles with a composition similar to the one recorded in this study after addition of 2 wt% Ag to an extruded Mg−8.5Gd−2.5Y−0.5Zr alloy.

Fig. 2d and e illustrates the respective inverse pole figure (IPF-Z, with Z//ED) map and GOS map of the extruded alloy in a plane perpendicular to ED. The (0001) pole figure of the extruded alloy in the TD-ND section is also provided in the corner of Fig. 2d, demonstrating that the majority of basal planes are inclined relative to ED. A concentrated basal pole with the maximum intensity of 2.7 shows that most of basal planes are arranged about 65° relative to ED (Fig. 2d). The corresponding grain size and misorientation angle distribution histograms are also depicted in Fig. 2f and g, respectively. The IPF map shown in Fig. 2d clearly demonstrates a recrystallized microstructure along with equiaxed grains, already observed in the SEM micrographs. The grain size distribution diagram illustrated in Fig. 2f presents a normal distribution with an average grain size of 7.5 μm. The GOS map result shown in Fig. 2e confirms the existence of a fully recrystallized microstructure with a high fraction of recrystallized grains (f_{REX} = 95%) for the extruded alloy, being well corroborated by the misorientation angle distribution histogram presented in Fig. 2g exhibiting a high fraction of HAGBs (f_{HAGBs} = 97%).

3.2. The microstructural features after SSE and ECAP

The microstructures of the processed samples after 1, 2, 4 and 6 passes of SSE and ECAP at 553 K are depicted by IPF maps in Fig. 3, and the corresponding grain size distribution diagrams, expressed in term of the area fraction of the grains, are provided in Fig. 4. The area-weighted average grain size ($d_{ave\,(weighted)}$) for each condition is also demonstrated in the distribution diagrams (Fig. 4). The standard error for a weighted mean value was calculated using Galloway method [31] for each case. It can be observed that after 1 pass of SSE and ECAP, the microstructure of both conditions contains coarse deformed grains. However, the size of the large un-DRXed grains in SSE-1P is much higher than those in the ECAP-1P condition, as shown in Fig. 3a and b. This is also discernible in Fig. 4a and b, where the grain size distribution of ECAP-1P shows a more pronounced accumulation of grains at smaller sizes. After 2 passes, the microstructures of the specimens processed by both SPD methods have experienced some changes. According to the IPF maps shown in Fig. 3c and d, both SSE-2P and ECAP-2P conditions possess coarse severely deformed grains surrounded by fine freshly DRXed grains. The emergence of sharp peaks at small grain sizes in the grain size distribution histograms in Fig. 4c and d for SSE-2P and ECAP-2P can also be interpreted as the proceeding of the DRX phenomenon throughout the entire microstructure, as the straining rises in both SSE and ECAP processes. However, a significant portion of the microstructure still contains the severely deformed coarse grains with substructures formed within them. This situation is even more pronounced for the SSE-2P condition, as the deformed grains seem much more elongated and even larger in size com-

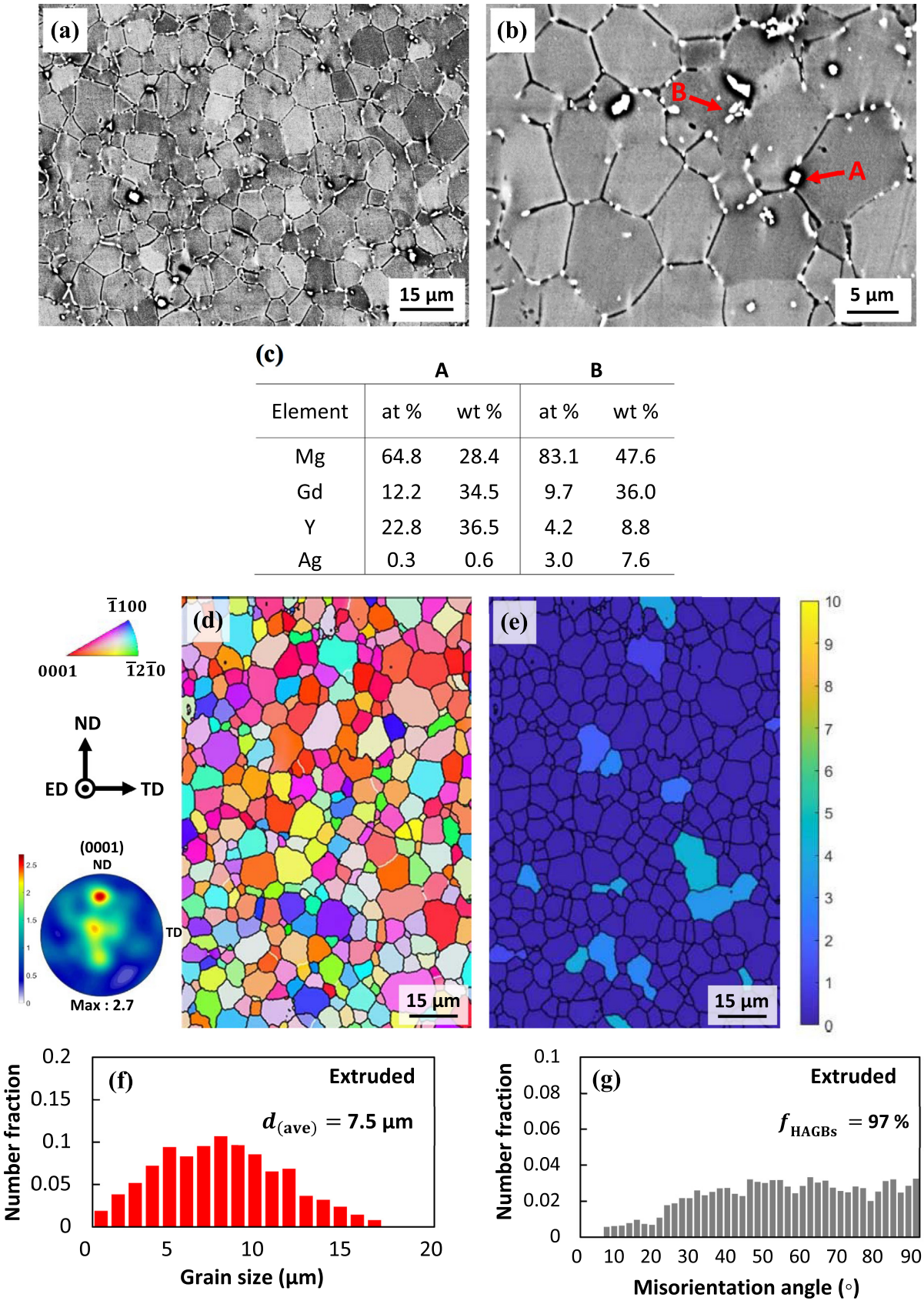

	A		B	
Element	at %	wt %	at %	wt %
Mg	64.8	28.4	83.1	47.6
Gd	12.2	34.5	9.7	36.0
Y	22.8	36.5	4.2	8.8
Ag	0.3	0.6	3.0	7.6

Fig. 2. SEM micrographs of the extruded alloy at different magnifications in a plane perpendicular to ED (a and b) and the EDS analysis results (c) for the particles "A" and "B" marked in (b); IPF map along with its corresponding (0001) pole figure (d) and GOS (e) map of the extruded alloy in a plane normal to ED, and the corresponding grain size (f) and misorientation angle (g) distribution diagrams obtained from the EBSD results.

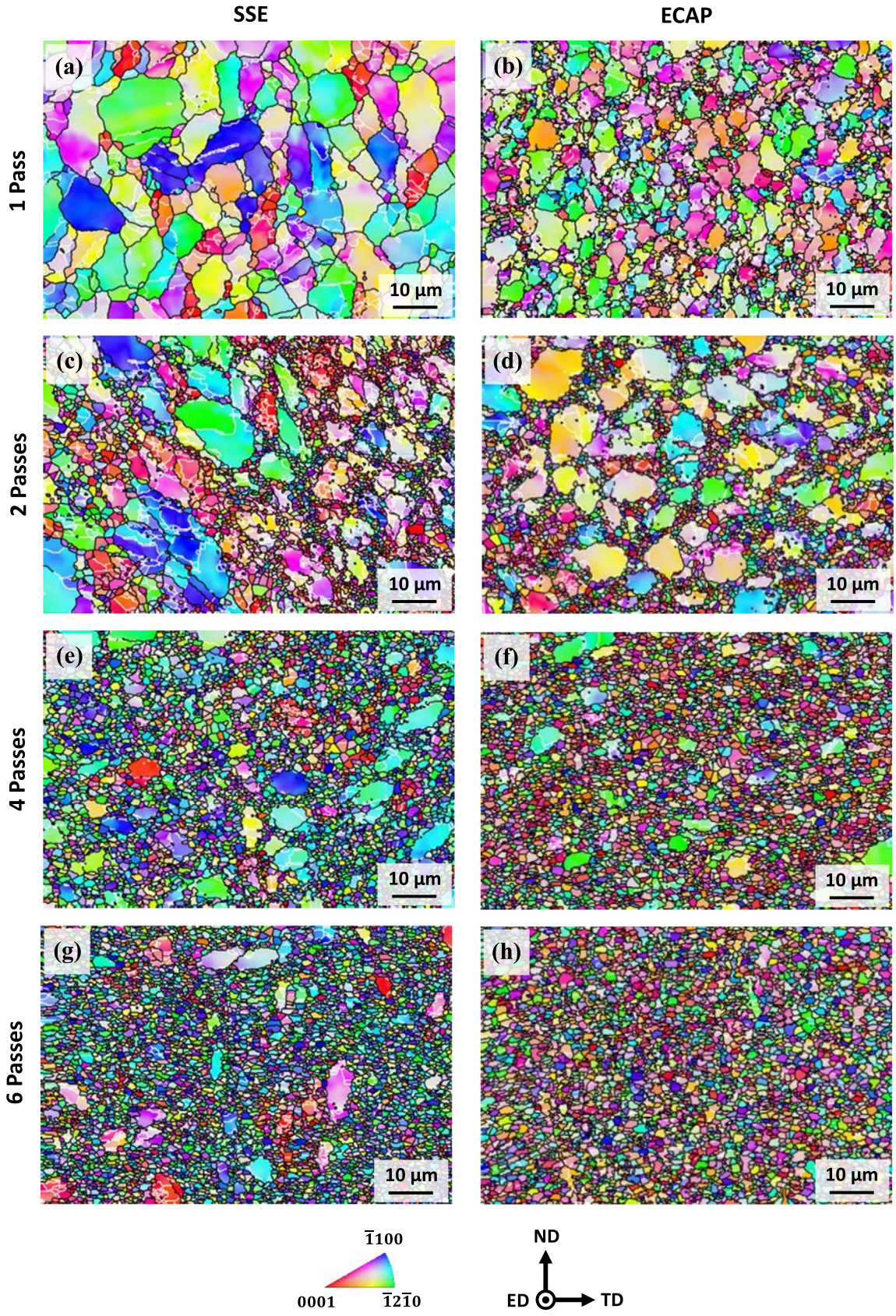

Fig. 3. IPF maps of the alloys processed for 1, 2, 4 and 6 passes of: SSE (a, c, e and g) and ECAP (b, d, f and h) at 553 K in a plane normal to ED.

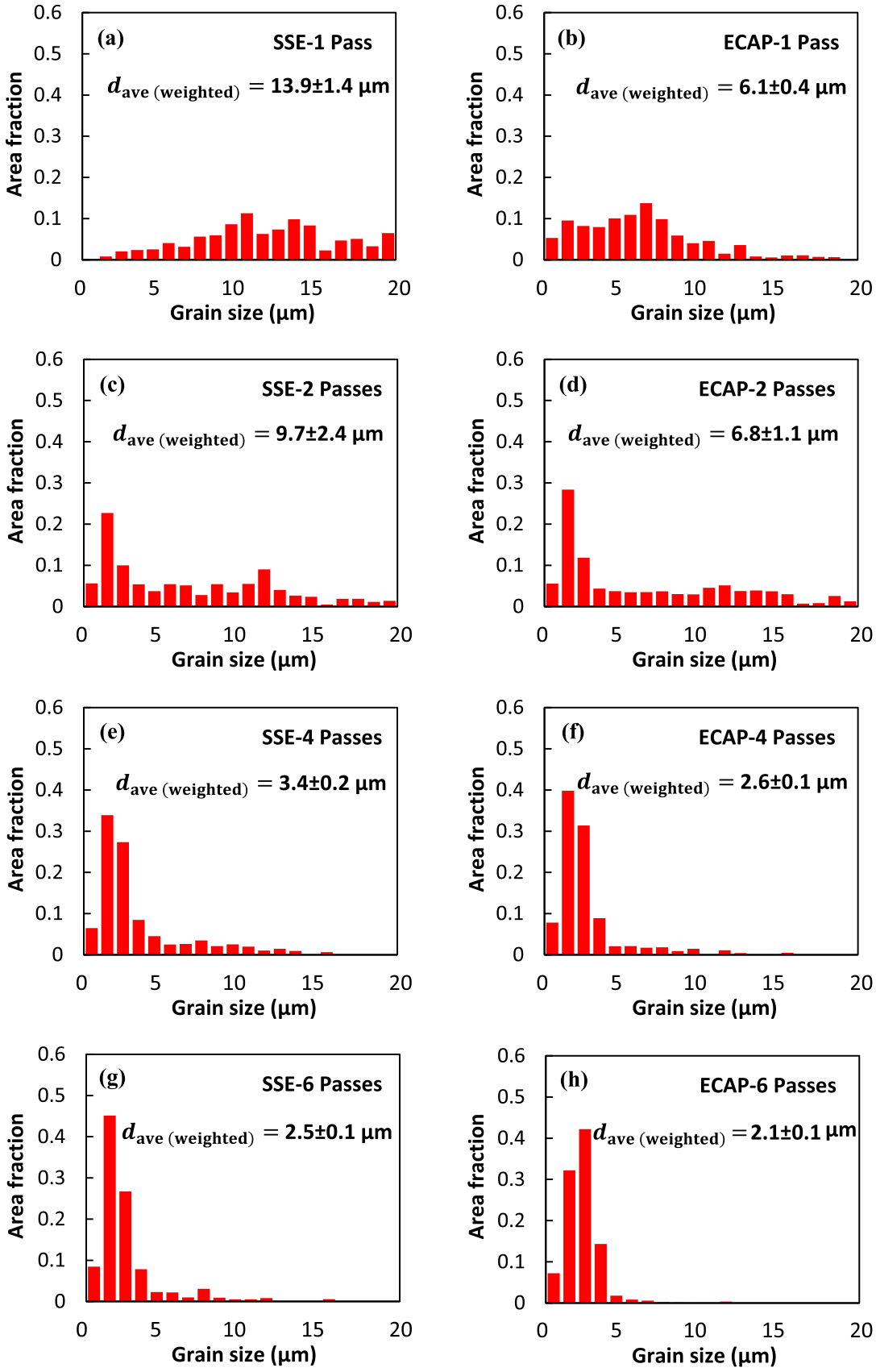

Fig. 4. Grain size distribution diagrams obtained from the EBSD results for the alloys processed after different passes of 1, 2, 4 and 6 by SSE (a, c, e and g) and ECAP (b, d, f and h).

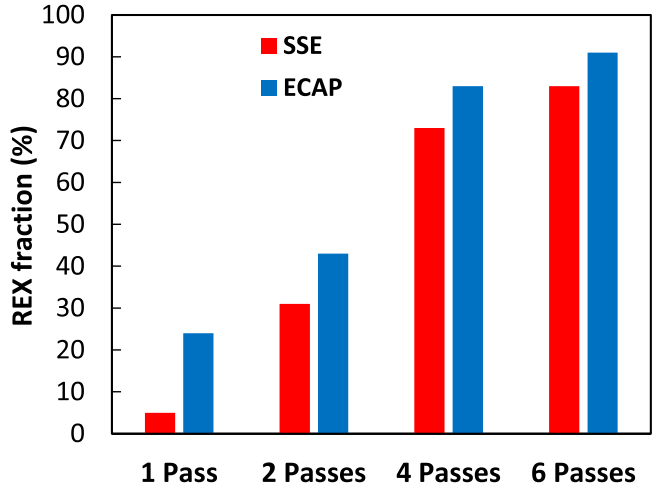

Fig. 5. Comparison of the recrystallization fraction after different passes of SSE and ECAP at 553 K.

pared to its counterpart specimen processed by ECAP. After 4 passes of SSE and ECAP, the microstructures of SSE-4P and ECAP-4P become much more homogenous according to the IPF maps exhibited in Fig. 3e and f. A similar trend can be observed by further increasing the number of passes from 4 to 6 for SSE-6P and ECAP-6P, achieving the most homogenous microstructures in this working condition for both processing methods (Fig. 3g and h). However, the ECAP-6P condition has exhibited a higher degree of homogeneity compared to SSE-6P, as there are still some large un-DRXed regions in the microstructure for the latter one. The significant rise in the peak value of the newly formed fine grains after 4 and 6 passes of SSE and ECAP is evident in the grain size distribution histograms of Fig. 4e–h. According to the EBSD results, the size of the newly formed fine recrystallized grains for both SPD methods were similar, so that the average values of 1.3 and 1.4 μm were recorded for the SSE-6P and ECAP-6P conditions, respectively.

The bar chart provided in Fig. 5 compares the faction of recrystallization for the alloy processed by different passes of SSE and ECAP. Considering the GOS criterion, the fraction of the newly recrystallized grains (f_{REX}) is 5% for SSE-1P and 24% for the ECAP-1P specimens (Fig. 5). This large gap between the recrystallization fractions after one pass will be discussed in Section 4.2. Recrystallization fractions of 31% and 43% are recorded for SSE-2P and ECAP-2P, respectively. It is clear that the fraction of the DRXed grains increased compared to those processed by 1 pass of ECAP and SSE. By increasing the pass number to 4, even more increment in the fraction of fine DRXed grains is observed, where it increased significantly to 73% and 83% for the specimens processed by SSE and ECAP, respectively. The recrystallization fraction of $f_{REX} = 83\%$ was obtained for SSE-6P, while in the ECAP-6P specimen a greater value of $f_{REX} = 91\%$ was obtained.

Fig. 6a–d shows the bright field TEM micrographs of the SSE-6P and ECAP-6P conditions at different magnifications. Both SSE and ECAP-processed alloys consist of fine DRXed grains decorated with some globular nano-particles mostly at the boundaries of the dynamically recrystallized areas. Some large un-DRXed regions were also detected in the microstructure of SSE-6P, as marked by red borders in Fig. 6a, which were not found for the one processed by 6 ECAP passes. This is in agreement with the presence of some large deformed grains that have not yet dynamically recrystallized even after 6 passes of SSE, as shown in IPF map of Fig. 3g. The higher magnification TEM micrographs provided in Fig. 6c and d display the bowing of some dislocation lines around the globular nano-particles. The EDS spectra and chemical composition of the nano-particles, obtained by TEM, are presented in Fig. 6e. The chemical composition of the globular nano-particles is close to that of the Mg_5Gd-type intermetallic compounds with a general form of $Mg_5(Gd,X)$, in which "X" refers to other alloying elements such as yttrium (Y) and silver (Ag) that can substitute Gd. The selected area electron diffraction (SAED) pattern taken from the $Mg_5(Gd,X)$ nano-particles is indexed with a FCC structure having a zone axis of $Z = [\bar{1}12]$ and the lattice parameter of $a = 2.21$ nm, as shown in Fig. 6f. Measurements showed these nano-particles had a size in the range of 60 to 380 nm with an area-weighted average diameter ($d_{P(ave)}$) of 237 and 225 nm for SSE-6P and ECAP-6P, respectively.

The misorientation angle histograms are exhibited in Fig. 7. After the first pass of SSE and ECAP, the corresponding misorientation angle distribution diagrams shown in Fig. 7a and b exhibit a distinct peak at small angles that is indicative of formation of LAGBs. The misorientation angle histograms after 2 passes of SSE and ECAP still exhibit a high fraction of LAGBs, as shown in Fig. 7c and d. By increasing the number of passes from 1 to 2, the fraction of HAGBs (f_{HAGBs}) for the alloy processed by SSE increases significantly from 56% to 63%; while it raises marginally from 70% to 72% for the one processed by ECAP (Fig. 7a–d). After 4 and 6 passes of SSE and ECAP, drastic changes are detected in the corresponding misorientation angle distribution diagrams (Fig. 7e–h). The abrupt increase of the fine DRXed grains and the subsequent decrease in the fraction of the large grains having LAGBs can also be easily observed in the misorientation angle histograms after 4 and 6 passes of SSE and ECAP. The sharp peaks at the lower misorientation angle values have faded out for the SSE-4P and SSE-6P conditions (Fig. 7e and g). A similar trend is observed for ECAP-4P and ECAP-6P as well (Fig. 7f and h). It is noticeable that for both SSE and ECAP, the greatest fractions of HAGBs are recorded for the highest applied strain (6 passes), where $f_{HAGBs} = 91\%$ and $f_{HAGBs} = 96\%$ were obtained for the SSE-6P and ECAP-6P conditions, respectively. It can also be inferred that after identical passes, the alloys treated via ECAP exhibited greater values of HAGBs compared to the one processed by SSE.

Fig. 8 illustrates the geometrically necessary dislocation (GND) density maps after different passes of SSE and ECAP, and their average value are compared for the two SDP techniques after different passages in the bar chart of Fig. 9. The trends of variation in the GND density values show that as

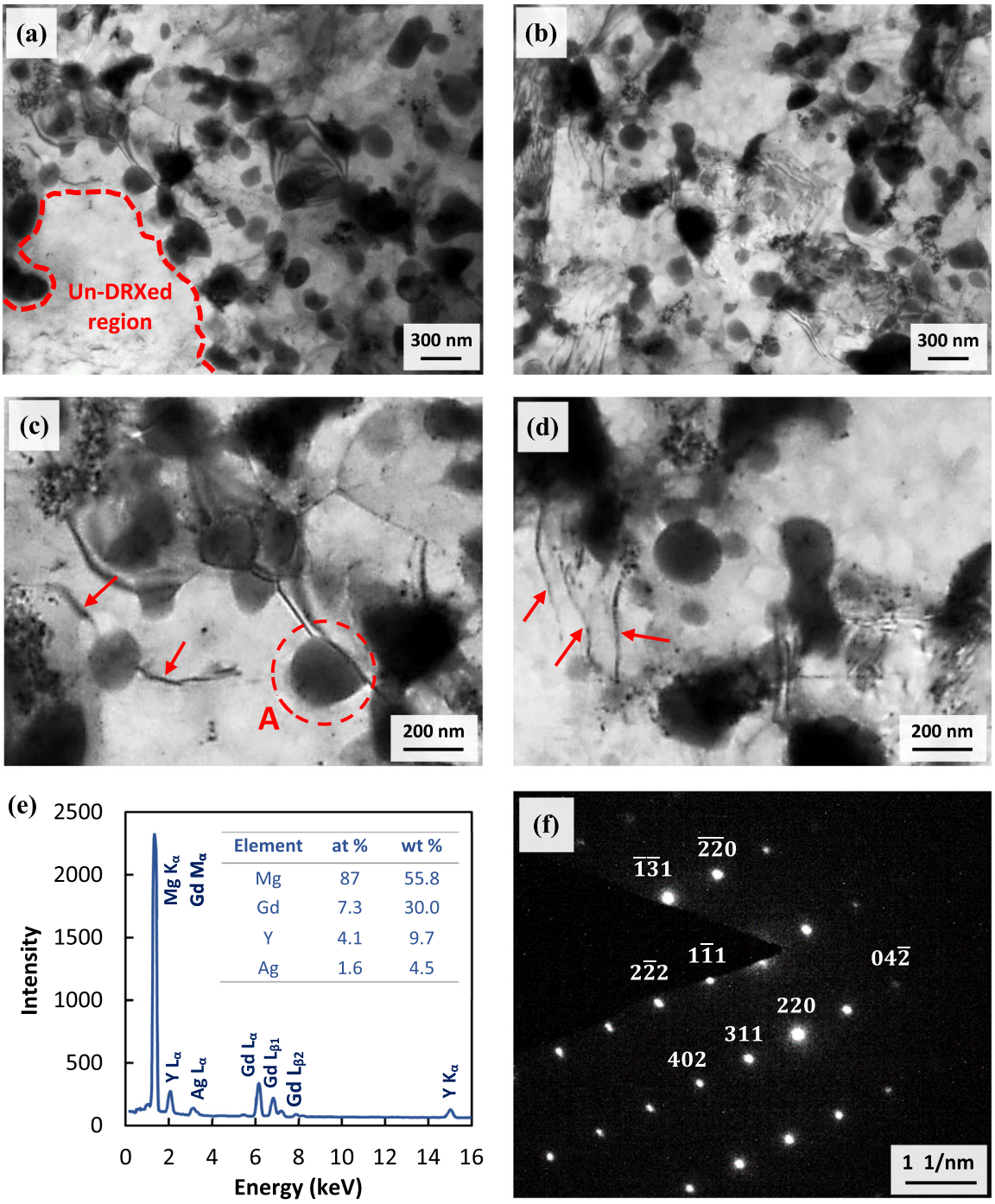

Fig. 6. Bright field TEM micrographs of the alloys after being processed by 6 passes of SSE (a) and ECAP (b) and their respective enlarged areas in (c) and (d), wherein the red arrows are pointing to the bowed dislocation lines around the nano-particles; the EDS analysis results (e) and also the SAED pattern (f) indexing an FCC structure with the zone axis of $Z = [\bar{1}12]$ from the globular shaped nano-particles chosen from location "A" marked in (c). (For interpretation of the references to color in this figure legend, the reader is referred to the web version of this article.).

the applied strain increases the average GND density values drop significantly compared to those for the early stages of processing for both SSE and ECAP. Moreover, after the same processing passes, the samples deformed by ECAP exhibited lower average GND density values in comparison to those processed by SSE.

3.3. Development of crystallographic texture during SSE and ECAP

Fig. 10 depicts textural evolution expressed in terms of pole figures for (0001) basal planes in the TD-ND surface. The crystallographic textures of the samples after 1 pass of

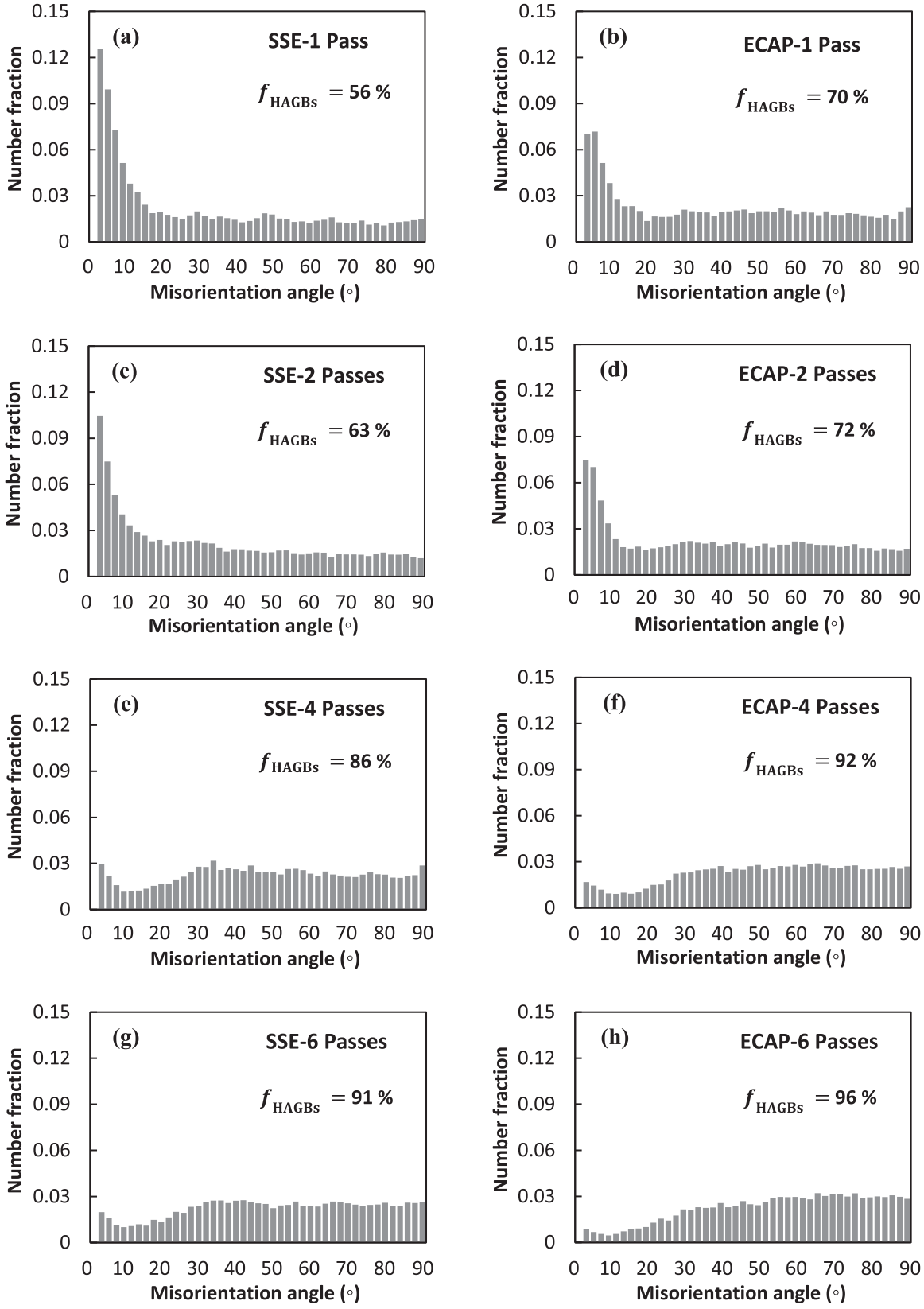

Fig. 7. Misorientation angle distribution diagrams obtained from the EBSD results for the alloys processed after different passes of 1, 2, 4 and 6 by SSE (a, c, e and g) and ECAP (b, d, f and h).

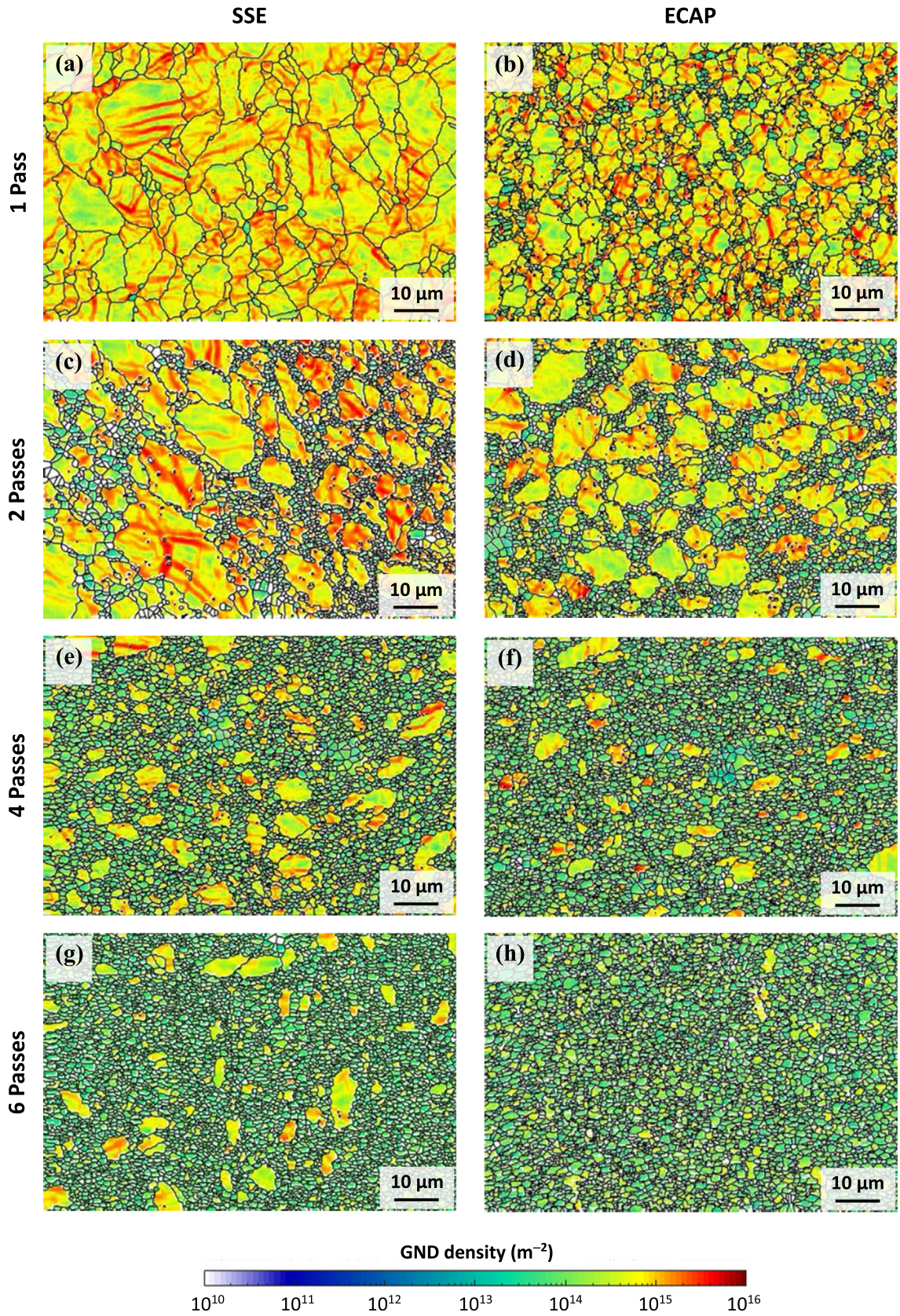

Fig. 8. GND density maps obtained from the EBSD data for the alloys processed after different passes of 1, 2, 4 and 6 via SSE (a, c, e and g) and ECAP (b, d, f and h) techniques at 553 K in a plane normal to ED.

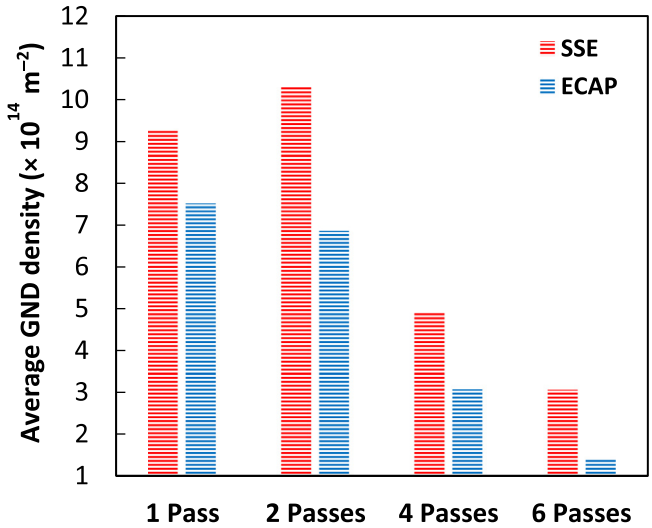

Fig. 9. Comparison of the average GND density values for the alloys processed through different passes of SSE and ECAP techniques at 553 K.

SSE and ECAP exhibit relatively scattered basal poles, with the highest maximum intensities of 6.1 and 5.7, respectively (Fig. 10a and b). It can be inferred that the pole of the basal planes for SSE-1P are inclined towards ND, while the basal poles for ECAP-1P are rotated away from ED. After 2 passes of SSE and ECAP, both conditions exhibited a more distinguished texture along with lower maximum intensities compared to those processed by only 1 pass (Fig. 10c and d). It is clear that the basal planes in SSE-2P are almost perpendicular to ND with a few degrees of deviation as shown in Fig. 10c, whereas ECAP-2P has demonstrated a texture with the basal planes inclined about 45° relative to ED, as shown in Fig. 10d. It seems that the angle between the poles of the basal planes and ED in SSE-2P has increased a few degrees compared to SSE-1P. By raising the pass numbers to 4 and 6, a much more concentrated and defined texture has emerged for the alloys processed through both SSE (Fig. 10e and g) and ECAP (Fig. 10f and h). In the case of SSE-4P and SSE-6P, two types of strong basal components with different positions are formed. The first type involves basal planes, the majority of which being parallel to ED with their poles aligned along ND. For convenience, this basal component is considered as "type-A" in this study from now on. The basal component "type-A" can be easily identified by the basal poles positioned at the northern-southern parts of the (0001) pole figures of SSE-4P and SSE-6P conditions in Fig. 10e and g, respectively. The second texture component developed in the samples processed by SSE is comprised of the basal planes rearranged again parallel to ED, but with their normal almost aligned in the transverse direction (TD), being called basal component "type-B". According to the (0001) pole figures of SSE-4P and SSE-6P in Fig. 10e and g, the texture component "type-B" is exhibited by the basal poles concentrated at the western-eastern regions of the pole figure maps.

For further verification of different texture components, formed after processing by SSE, the IPF of SSE-6P in three main directions of ED, TD and ND are presented in Fig. 11a, where the results are in excellent accordance with the (0001) basal pole figures. The basal component of "type-A" is well demonstrated by accumulation of the basal poles with a [0001] direction in the IPF of direction ND. Similar justification can be made for the basal component "type-B" for the one with TD axis, as shown in Fig. 11a. On the other hand, the texture component of ECAP-6P is entirely unique and differs from those developed for alloys processed by SSE. It is also worth mentioning that both of SSE-6P and ECAP-6P alloys have exhibited the lowest maximum intensities among all the processed conditions. According to the (0001) pole figures in Fig. 10d, f and h, the basal planes are rearranged with an approximate deviation angle of about 45° from the main processing direction of ED. However, the positions of their poles have been changed relative to the transverse direction continuously as the number of ECAP passes increases.

In order to reach a better understanding of how the crystallographic texture has evolved differently after 6 passes of processing by SSE and ECAP, a schematic illustration regarding the position of HCP crystals relative to the shear planes and the three main directions (i.e., ED, TD and ND) of both SPD methods is presented in Fig. 12. The predefined basal components of "type-A" and "type-B" developed in SSE-6P are well distinguished and introduced in Fig. 12a, and the position of the corresponding basal planes are determined with respect to both shear planes and shear direction imposed during the SSE process. It is evident that the basal planes of the texture component "type-A" are parallel to the shear plane of the SSE process, which are positioned on ED-TD surface. This is not the case for the component "type-B", in which the basal planes are perpendicular to the shear planes of SSE. In the case of ECAP-6P, the way in which the basal planes are rearranged relative to the geometrical shear plane in the intersection of the channels in ECAP is exhibited in Fig. 12b.

3.4. Mechanical properties after SSE and ECAP

Uniaxial compression testing along ED was carried out to assess the mechanical properties of the alloy in the extruded condition and after different passes of SSE and ECAP. The obtained compressive true stress–strain curves are presented in Fig. 13. The corresponding mechanical properties such as compressive yield stress (CYS), ultimate compressive strength (UCS), and fracture strain (ε_f) are summarized in the comparative diagrams of Fig. 14. It is evident that the extruded condition has the lowest values of CYS and UCS among all tested conditions (Figs. 13 and 14). It can be deduced that by raising the number of passes, the CYS and UCS of the samples processed by either of SSE or ECAP have increased continuously, those of the SSE process being always higher than ECAP when compared at same number of passes. In contrast to the strength, fracture strain decreases with increasing the pass numbers in SSE and ECAP, those of ECAP being higher than the SSE process (Figs. 13 and 14).

In order to seek the origins of the discrepancies in the mechanical properties of the alloys after SSE and ECAP, the role

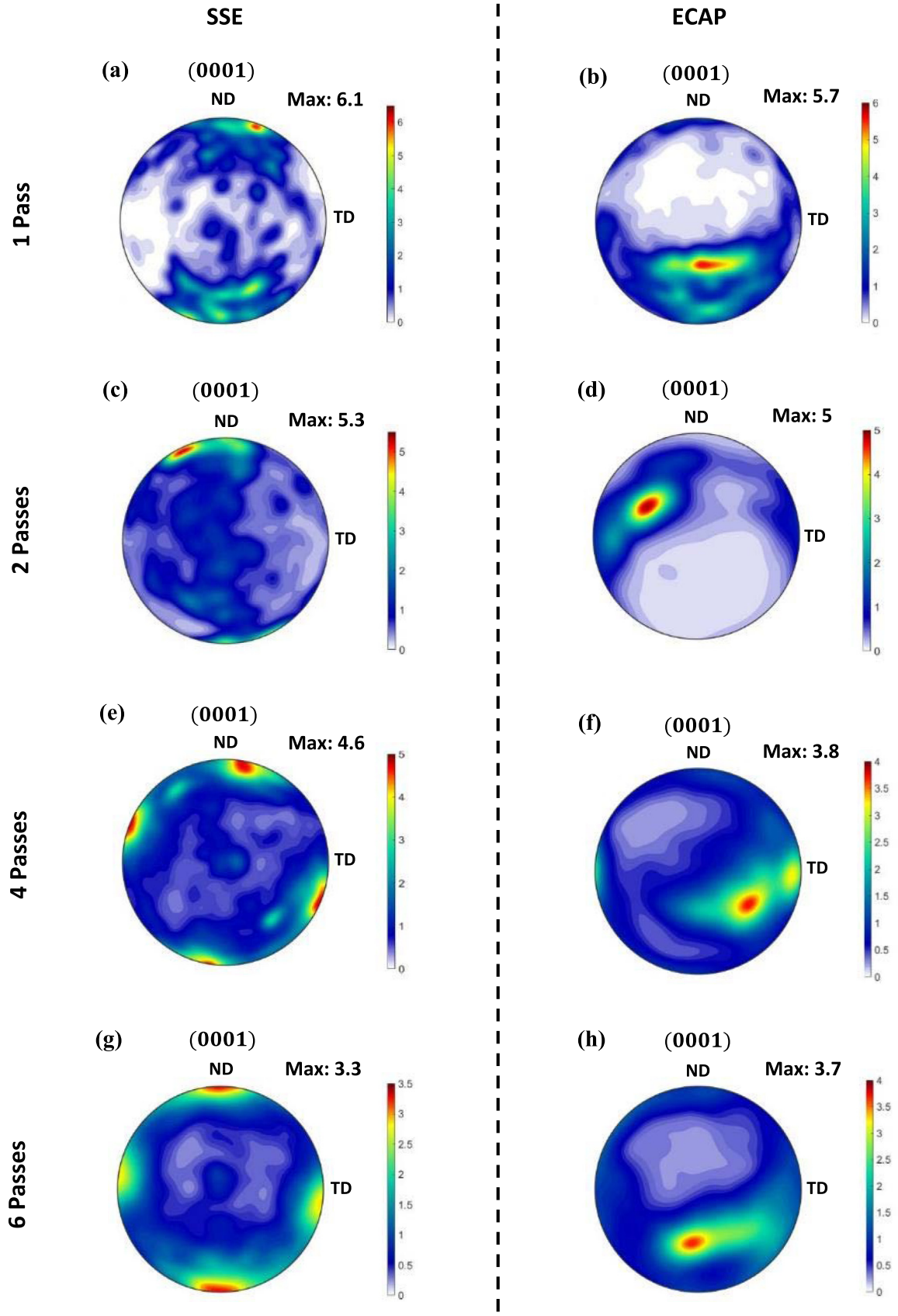

Fig. 10. Pole figures of the (0001) basal planes in the TD-ND section obtained from the EBSD results for the alloys processed after different passes of 1, 2, 4 and 6 by SSE (a, c, e and g) and ECAP (b, d, f and h).

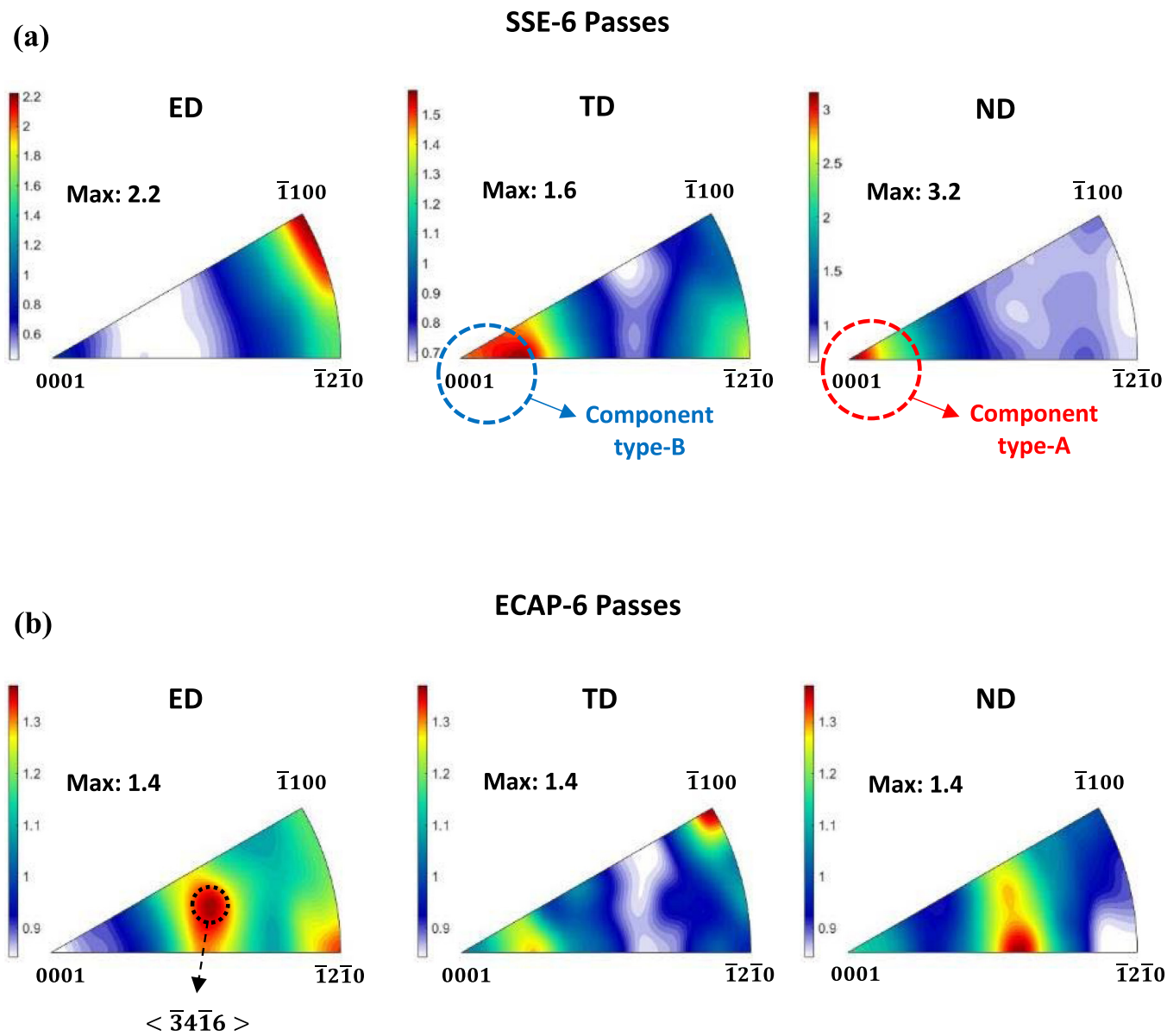

Fig. 11. Inverse pole figures in the main three specimen axis of ED, TD and ND obtained from the EBSD results for the alloys processed after 6 passes of SSE (a) and ECAP (b) techniques.

of different crystallographic textures was investigated through considering the contribution of the most probable slip system, i.e., basal planes. Accordingly, Schmid factor (SF) histograms of the (0001) $<11\bar{2}0>$ basal slip system with the loading direction parallel to ED obtained from EBSD results are provided in Fig. 15 for the conditions processed by 2, 4 and 6 passes of SSE and ECAP. One would observe the noticeable difference in the distributions of the Schmid factors of basal planes for the SSE and ECAP. Obvious sharp peaks are formed close to the greatest SF value of 0.5 for the ECAP-2P, ECAP-4P and ECAP-6 conditions, as depicted in Fig. 15b, d and f respectively. The SF distribution histograms of the SSE conditions, however, show an almost uniform pattern with no specific accumulation at high SF values. Moreover, the average values, $SF_{(ave)}$, are noticeably greater for the conditions processed by ECAP compared to ones in SSE at the same processing passes. The highest $SF_{(ave)} = 0.38$ was recorded for ECAP-6P, while for SSE-6P an $SF_{(ave)}$ value of 0.22 was obtained, which is the least average Schmid factor achieved among all the conditions processed by the two SPD techniques in this study.

4. Discussion

4.1. Grain refinement and dynamic recrystallization after SPD processing

The microstructural studies by EBSD analysis showed that both SPD techniques are efficient in grain refinement via DRX after 6 passes of processing at 553 K (Figs. 3 and 5). In

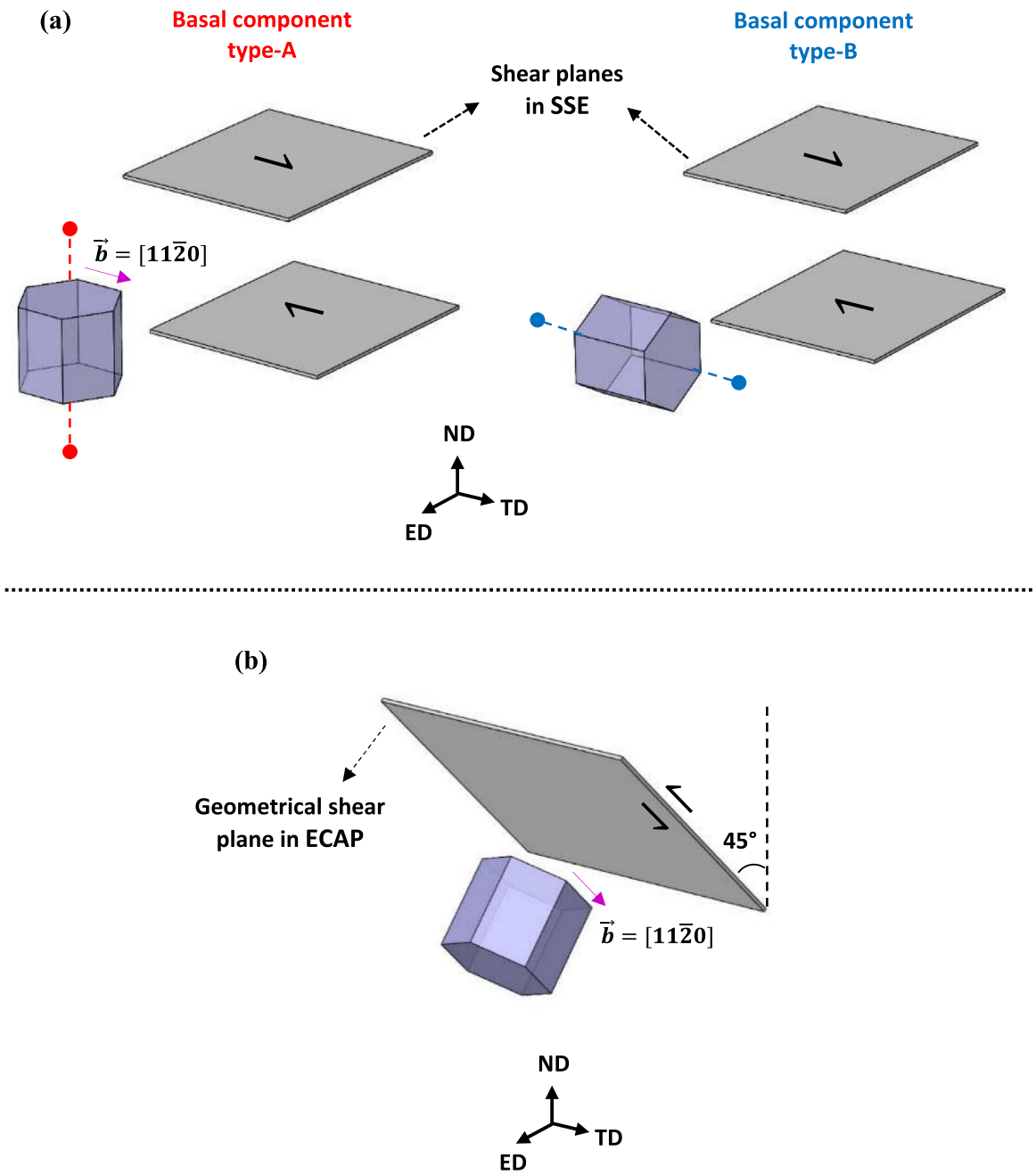

Fig. 12. Schematic presentation of how the HCP crystals are realigned relative to the shear planes after 6 passes of both SSE (a) and ECAP (b) techniques.

the early stages of SSE and ECAP, both conditions have exhibited high fractions of LAGBs developed within the large heavily deformed grains, and this situation is even more pronounced in SSE-1P and SSE-2P compared to those processed by ECAP (Fig. 7). After 1 pass of SSE and ECAP, an equivalent mean strain of about ∼ 1 is imposed on the workpiece in both methods, leading to an increase in the density of stored dislocations. Since deformation has been performed at the relatively high temperature of 553 K, the accumulated dislocation tangles would easily rearrange to arrays of substructures to form LAGBs and/or other types of geometrically necessary boundaries (GNBs) in the interior of the large original deformed grains via dislocation climb and cross slip during the occurrence of dynamic recovery (DRV) [32,33]. That is why a steep rise in the low values (< 15°) of misorientation angle distribution diagrams in the early stages of straining for both SSE-1P and ECAP-1P has been developed (Fig. 7a and b).

After 2 SSE and ECAP passes, although dynamic recrystallization has proceeded significantly for each case, there are still a noticeable fraction of LAGBs remaining in the microstructure, as shown in the IPF maps (Fig. 3c and d) and also in the corresponding misorientation angle distribution histograms in Fig. 7c and d. This implies that in the interme-

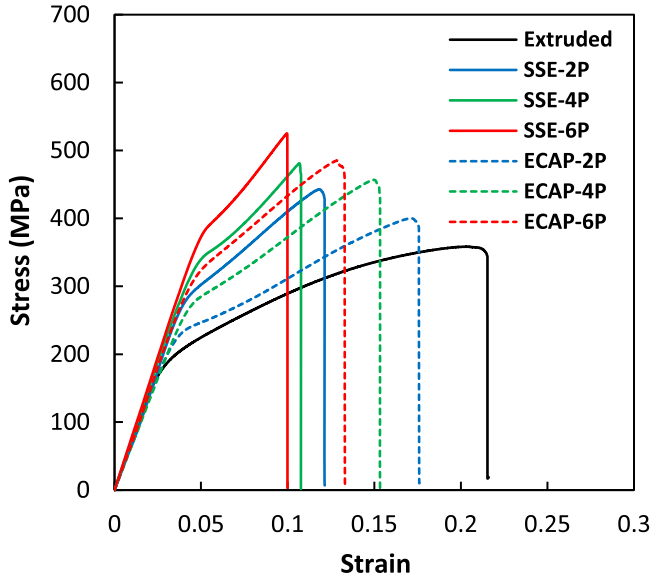

Fig. 13. True stress-strain curves obtained from the compression tests performed in the ED direction for the alloys in the extruded state and after different passes of 2, 4 and 6 processed by both SSE and ECAP techniques.

diate stages of processing, both DRV and DRX are operative by further straining in either SPD scenarios. That is why the microstructures are in their most heterogeneous state, i.e., partially recrystallized, for the SSE-2P and ECAP-2P samples. However, the most drastic changes take place by increasing the number of passes to 4 and 6 in both SSE and ECAP. It is evident that by raising the imposed strain in passes 4 and 6, the fractions of recrystallization and HAGBs have continued to increase significantly. The noticeable drop of the sharp peaks at the low values of misorientation angle, which are attributed to LAGBs, can be clearly observed in the distribution diagrams of Fig. 7e–h. This could be concomitantly correlated to the significant proceeding of DRX for large strains imposed by each SPD process. Therefore, at the early stages of deformation where the fraction of LAGBs is abundant, continuous dynamic recrystallization (CDRX) which is accompanied by a persistent and massive conversion of low angle boundaries to high angle boundaries as the straining raises during the deformation [34–36], could be considered as the operative DRX mechanism in both SSE and ECAP at 553 K.

The GND density distribution results obtained from EBSD studies depicted in Fig. 8 also shows a progressive consumption of subgrain boundaries or other GNBs that is also in accordance with the reduction of LAGBs by increasing the strain. The decrease in the average GND densities for alloys processed by ECAP seems to have occurred more efficiently than the ones treated via SSE after the same pass numbers (Fig. 9), which will be explained through the higher equivalent strain rate for ECAP (see Section 4.2).

The EBSD results shows also that new LAGBs stopped being produced with increasing number of passes to 4 and 6. Furthermore, grain subdivision is not apparent inside the initial grain structure; new grains only appear at grain boundaries. Thus, discontinuous nucleation and growth of new grains at the former grain boundaries could also explain the disappearance of LAGBs at the large strains, as they would be consumed by the motion of newly created HAGBs. The noticeable reduction in the amount of LAGBs and in the GND density with increasing number of passes to 4 and 6 leads to the conclusion that DDRX starts becoming active at large strains. Fine new recrystallized grains keep forming along the serrated pre-existing boundaries through localized bulging and boundary migration [37], manifesting a necklace-type feature (Fig. 3). As the deformation proceeds, the recrystallized grains formed by DDRX in the boundary regions extend to the central areas of the deformed parent grains and consume almost the entire microstructure leaving behind volumes having lower density of dislocations [34]. This massive progression of DDRX sweeps away the severely deformed grains along with the stored dislocations within them [38], leading to the sharp decrease in the fraction of LAGBs at high straining levels accordingly. Hence, it is concluded that DDRX operates during processing through both SPD methods, with a potential contribution of CDRX at the early stages.

The $Mg_5(Gd,X)$ nano-sized particles, shown in the TEM micrographs of Fig. 6, have been formed through dynamic precipitation as the DRX proceeded during straining in both SPD processes. The formation of $Mg_5(Gd,X)$ nano-particles via dynamic precipitation at high temperature working conditions have been reported for various Mg−Gd−Y alloys [39–41]. The absence of the $Mg_5(Gd,X)$ nano-particles in the large un-DRXed regions of the SSE-6P alloy, as shown in the bottom left corner of the TEM micrograph of Fig. 6a, totally conveys the idea of their formation through dynamic precipitation during DRX after being processed by both SPD techniques at 553 K. The emergence of these Mg_5Gd-type nano-particles through dynamic precipitation is a strain-induced phenomenon that is encouraged via development of dislocation boundaries or other types of deformation-induced structures during hot working as they could provide fast diffusion paths and act as potential sites of heterogeneous nucleation for new intermetallic phases. This could be in accordance with the development of LAGBs and dislocations within the interiors of the deformed grains.

4.2. Effect of strain path on the characteristic features of the microstructure

Although the same dominant dynamic recrystallization mechanisms occur during both of the SPD treatments at 553 K, the rate by which it proceeds by increasing the strain has been shown to be different for SSE and ECAP according to the microstructural examinations performed through EBSD studies. In other words, the kinetics of evolutions in the microstructural characteristics such as the fractions of recrystallization and HAGBs were more pronounced for the alloys processed by ECAP (Fig. 5). The root of such discrepancy in the rate of microstructural evolutions for SSE and ECAP must be explored in different equivalent strain rates of these techniques as the other deformation parameters are identical. For the SSE process used here, the equivalent strain rate ($\dot{\varepsilon}^{x}_{eq,\ \mathrm{SSE}}$)

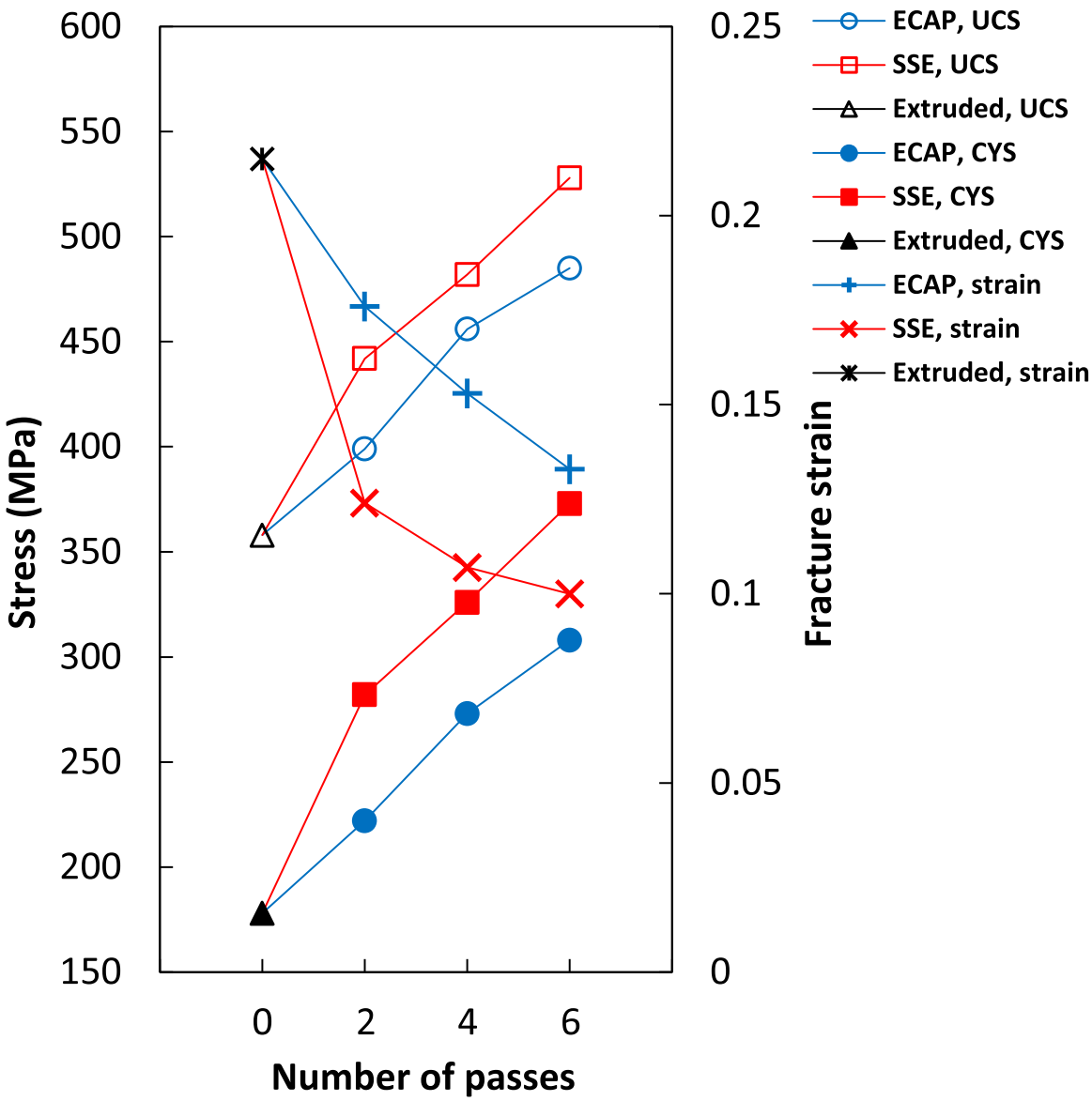

Fig. 14. Comparison of the compressive yield stress, ultimate compressive strength and fracture strain obtained from the compression test results for the alloys in the extruded state and after different passes of processing by SSE and ECAP.

as a function of distance "x" from the inlet of SSE channel would be obtained as follows [42]:

$$\dot{\varepsilon}^{x}_{eq,\mathrm{SSE}} = \begin{cases} \frac{16\tan(\alpha_{\max})}{\sqrt{3}L^2} x \frac{dx}{dt} & 0 \le x \le \frac{L}{4} \\ -\frac{16\tan(\alpha_{\max})}{\sqrt{3}L^2}(x-\frac{L}{2})\frac{dx}{dt} & \frac{L}{4} \le x \le \frac{L}{2} \\ \frac{16\tan(\alpha_{\max})}{\sqrt{3}L^2}(x-\frac{L}{2})\frac{dx}{dt} & \frac{L}{2} \le x \le \frac{3L}{4} \\ -\frac{16\tan(\alpha_{\max})}{\sqrt{3}L^2}(x-L)\frac{dx}{dt} & \frac{3L}{4} \le x \le L \end{cases} \quad (1)$$

where L is the effective length of the deformation channel that is equal to 60 mm in this study, $\frac{dx}{dt}$ is the pressing velocity or ram displacement rate, which was chosen to be 0.1 mm s^{-1}. According to Eq. (1), the equivalent strain rate for SSE varies with the ram displacement or the distance "x" from the inlet of deformation channel periodically. In SSE with the maximum distortion angle of $\alpha_{max} = 45°$ and considering the other geometrical parameters, the greatest equivalent strain rate of 3.8×10^{-3} s^{-1} is achieved. In a similar manner, the equivalent strain rate for ECAP technique ($\dot{\varepsilon}_{eq,\mathrm{ECAP}}$) could be calculated through geometrical parameters of the process accordingly as bellow [43]:

$$\dot{\varepsilon}_{eq,\mathrm{ECAP}} = \frac{\bar{\varepsilon}_{\mathrm{ECAP}}}{\Delta t} = \frac{2\bar{\varepsilon}_{\mathrm{ECAP}}\, v}{\psi a}.\cos^2\left(\frac{\pi - \phi - \psi}{2}\right) \quad (2)$$

where Δt is the required elapsed time for a hypothetical element to pass through the main deformation zone located in the corner of the ECAP die, where the two channels intersect, v is the ram displacement rate that is equal to 0.1 mm s^{-1} identical to the one chosen for SSE, a is the width of the workpiece having a square cross section and is equal to 10 mm, $\bar{\varepsilon}_{\mathrm{ECAP}}$ is the imposed strain per each pass of ECAP, ϕ and ψ are the same parameters as defined earlier. Accordingly, for ECAP with the predefined geometrical and process-

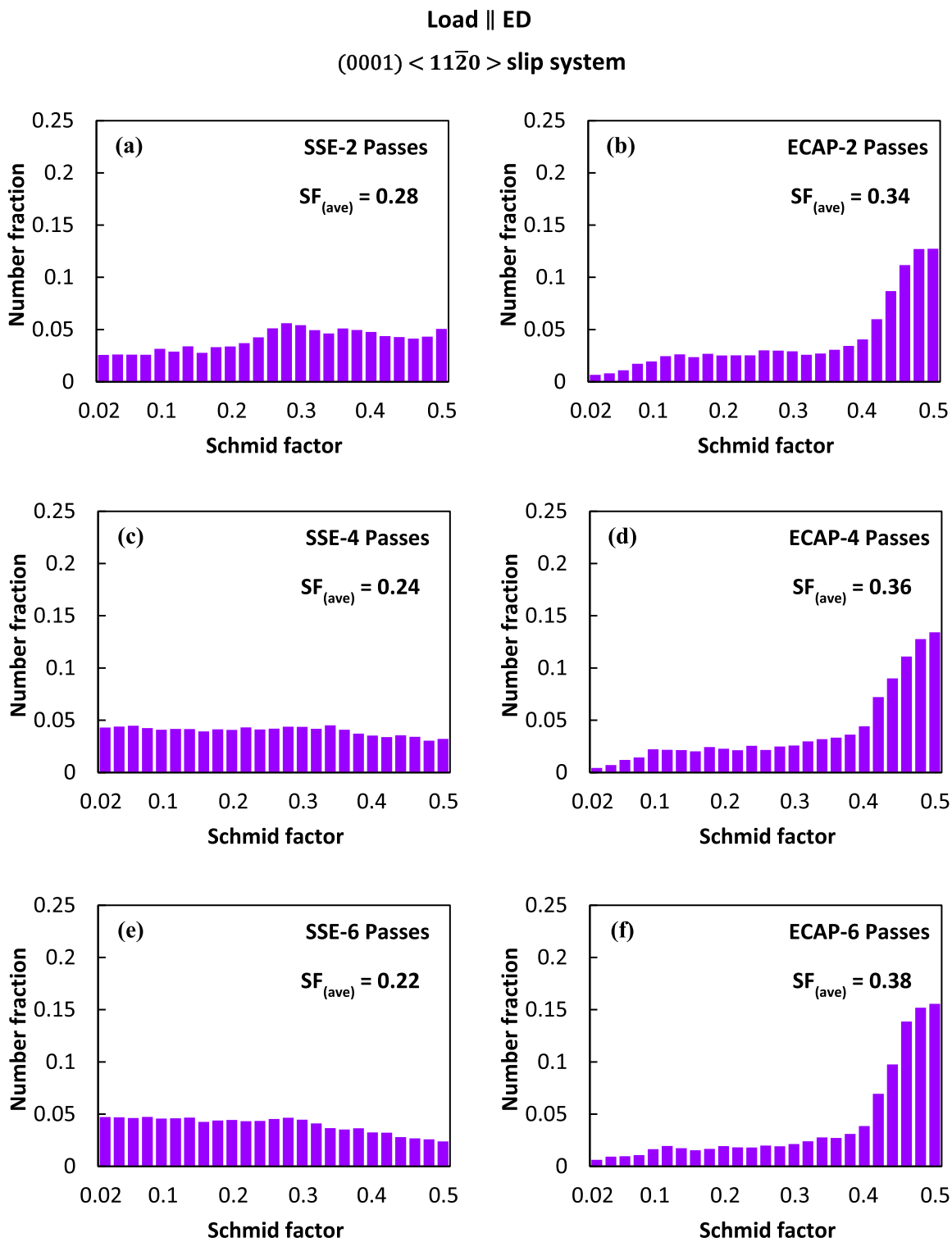

Fig. 15. Schmid factor distribution diagrams of the (0001) < 11$\bar{2}$0 > basal slip system with the loading direction parallel to ED obtained from the EBSD results for the alloys after being processed by 2, 4 and 6 passes of SSE (a, c and e) and ECAP (b, d and f).

ing parameters, the equivalent strain rate is calculated to be a constant value of 3.9×10^{-2} s^{-1} that is about 10 times greater than the maximum corresponding value obtained for SSE.

Some of the microstructural features were found to be quite different, especially at the early stages of straining after 1 and 2 passes of processing for SSE and ECAP. Two major differences that are rather noticeable are as follows. First, the ECAP-1P condition has already undergone DRX with a recrystallization fraction of f_{REX} = 24% (Fig. 5). This can be identified via the emergence of fine equiaxed grains mostly decorated at the sites of pre-existing grain boundaries, as de-

picted in Fig. 3b. In contrast, it seems that DRX has not even begun in the SSE-1P alloy, and the microstructure is comprised of large heavily deformed grains with a lower fraction of HAGBs (56%) compared to $f_{\mathrm{HAGBs}} = 70\%$ for ECAP-1P alloy (Fig. 7). Secondly, according to the EBSD data, the size of the coarse deformed grains in the case of ECAP-1P, with an average value of $d_{\mathrm{DEF(ave)}}$ equal to 4.5 μm, was two times smaller than the one for SSE-1P alloy with a value of $d_{\mathrm{DEF(ave)}} = 9.3$ μm as it is deduced from the IPF maps of Fig. 3a and b. This can be attributed to the greater progression of DRX in ECAP-1P alloy and the fragmentation of the initial parent grains in the extruded state to finer ones after 1 pass of processing through occurrence of DRX. Moreover, as the rate of deformation in SSE is much lower than of ECAP, the workpiece is exposed to heating during straining in the deformation channel for a longer time, leading to more extensive dynamic grain growth in SSE-processed alloys finally.

However, the main question regarding how strain rates can override the kinetics of dynamic restoration processes in the cases of SSE and ECAP still remains. In studying a strain rate-sensitive plastic flow, it is customary to attest the strain rate of plastic deformation ($\dot{\varepsilon}_P$) in terms of density of moving dislocations on the basal plane (ρ) and their average velocity ($\bar{\upsilon}$) [44]. As a result, a raise in the strain rate of deformation would lead to a subsequent increase of dislocations density through their multiplication at the principal sources of dislocation production such as grain boundaries and/or second phase particles. The augmented pile-up of dislocations and increase in their density as a result of raising the deformation rate could lead to more intensive misorientation gradients in the grains interior and also formation of substructures locally, and this would be interpreted as higher stored energy [45–47]. This reinforced stored energy would provide the extra driving force to advance dynamic restoration processes with an enhanced pace when increasing the strain rate. As a result, the occurrence of DRV would proceed with an accelerated rate in the early stages of straining in ECAP technique rendering a transition to initiation of DRX much sooner than the ones processed by SSE. That is why after an almost identical level of imposed strain at each pass, the alloys treated via ECAP have exhibited greater percentage of recrystallization. It is also noteworthy to mention the role of strain reversing during SSE process as a complimentary effect to reduce the necessary driving force and tendency for the occurrence of DRX in the SSE-processed alloys through elimination of dislocations. Such interpretation associated with the strain reversal effect was recently been presented by Sayari et al. [48], where lower fractions of HAGBs and recrystallization was reported for a pure Mg processed by SSE compared to the ones treated by ECAP after identical number of passes at 523 K.

4.3. Effect of strain path on the crystallographic texture

Since the mode of deformation was simple shear in both cases, the observed difference in their crystallographic texture stemmed from different strain paths. Due to different geometrical tool design, shear planes are positioned in different manners with respect to the main pressing direction, as shown schematically in Fig. 12. It was revealed that after large amounts of strain in 6th pass, the basal planes in both of the SPD processes have been realigned to become parallel to their own peculiar shear planes. According to the inverse pole figures depicted in Fig. 11, different configurations of HCP crystals relative to ED can be observed for the two processes after 6 passes. The normal to the prismatic planes, i.e., $\langle\bar{1}100\rangle$ direction, is parallel to ED for most of the grains in the SSE-6P condition (Fig. 11a), while in the case of ECAP-6P this is the $<\bar{3}4\bar{1}6>$ direction that is positioned along ED (Fig. 11b).

Development of texture component "type-A" in the pole figures of (0001) basal planes for alloys processed by SSE implies that the basal planes have become rearranged parallel to the hypothetical shear planes, laying in the ED–TD surface. This has been clearly shown in both the inverse pole figure of direction ND in Fig. 11a and in the schematic illustration in Fig. 12a. In other words, the formation of component "type-A" for the alloys processed by SSE is attributed to the activity of basal slip system. However, such a conclusion cannot be drawn for the texture component "type-B", as the basal planes are rearranged almost perpendicular to the shear direction, and also are completely out of alignment with respect to the shear planes in SSE schematically sketched in Fig. 12a. Moreover, the emergence of texture component "type-B" cannot be simply attributed to the activity of non-basal slip systems, as the prerequisite for such interpretation is that these planes must be positioned parallel to the shear plane of SSE in the ED–TD surface. That is why in our previous work [25], development of the basal component of "type-B" was suggested to be a direct result of rotating the workpiece for 90° around ED between the consecutive passes during processing by SSE. In other words, the texture component "type-B" can be considered as a component "type-A", which has been rotated 90° around the extrusion direction of SSE process. To support our argument, the readers are referred to the basal pole figure of SSE-1P alloy displayed in Fig. 10a. As it is evident, there is no sign of "type-B" component poles in the western-eastern regions of the (0001) pole figure map, as there has not been any specimen rotation around ED in the first processing pass. Similar basal components of "type-A" and "type-B" have been also observed for an Mg−6Gd−3Y−0.5Ag alloy [28] and also for two binary magnesium alloys of Mg−Gd and Mg−Al [49], all of them being processed by SSE at 553 K under route C.

In ECAP, however, a strong single-type crystallographic texture component with the basal planes mostly rearranged about 45° relative to the ED is achieved, as can be observed in the (0001) pole figures of Fig. 10, and also schematically illustrated through the position of HCP crystals for ECAP-6P in Fig. 12b. This configuration of basal planes being deviated about ∼ 45° away from the main processing direction (ED) for an ECAP process with a die angle of $\phi = 90°$ operating under processing route of B_C has been known as a common crystallographic feature of ECAP technique in the literature,

and has been observed in various Mg alloys [50–52] all of which confirming the role of basal slip system in this regard.

4.4. Effect of strain path on the mechanical response

Regarding the compression testing results, processing through both SSE and ECAP leads to improving the CYS and UCS values, compared to one in the extruded condition. The observed enhancement increases by raising the pass numbers in both SPD cases, so that the highest corresponding values were obtained for the alloys processed after 6 passes. By increasing the SPD pass numbers, the continuous rise in the percentage of freshly developed fine DRXed grins along with formation of $Mg_5(Gd,X)$ nano-particles via dynamic precipitation led to a progressive improvement of the CYS of the SPD-treated alloys through grain boundary strengthening (Hall-Petch effect) and second phase particle strengthening (Orowan mechanism), respectively.

Further straining in both SSE and ECAP increase the percentage of fine DRX grains, and the effect of grain boundary strengthening becomes more pronounced due to the progressive rise in the density of HAGBs. For a heterogeneous partially DRXed microstructure, the contribution of recrystallized regions with refined grain size to the yield stress can be considered by incorporating the fraction of fine recrystallized grains (f_{REX}) into the prominent Hall-Petch relationship through the rule of mixture [53]. This approach has been adopted [54] to take into account the role of fine DRXed regions in improving the yield stress of different extruded Mg−2Sn−2Ca alloys.

Similar scenario may be considered for the Orowan strengthening mechanism, in which the $Mg_5(Gd,X)$-type nano-particles could take part. Since these particles are dynamically precipitated out of the Mg matrix after experiencing large strains concomitantly with the occurrence of dynamic recrystallization during SSE and ECAP, the progressive rise in percentage of DRXed regions would result in corresponding increase in volume fraction of $Mg_5(Gd,X)$ nano-particles accordingly. Thus, the contribution of Orowan strengthening would proceed to become more pronounced at higher pass numbers. According to the respective high magnification TEM micrographs of Fig. 6c and d for SSE-6P and ECAP-6P conditions, bypassing of $Mg_5(Gd,X)$ nano-particles by the bowed segments of the dislocation lines is evident, implying the effectiveness of these nano-particles in trapping and hindering the dislocations glide during straining.

Despite the effectiveness of both the SPD methods to improve the strength of the alloys relative to the as-extruded condition, the ECAP-processed conditions showed lower values of CYS and UCS when compared to the SSE-processed ones at a given pass number (Figs. 13 and 14). The discrepancy in the mechanical response of the alloys processed by SSE and ECAP should be interpreted on the basis of different crystallographic textures. Since the loading direction in the uniaxial compression is parallel to ED (Fig. 1), it can be declared that the majority of basal planes in the ECAP-processed conditions are inclined about 45° relative to the compressive loading axis (Figs. 10 and 12). This kind of configuration for basal planes in Mg alloys is considered as the easy orientation, which favors the yielding and activation of basal slip system [55].

According to Schmid law, as the SF value approaches its ideal maximum value of 0.5, like the cases of the alloys processed by ECAP in this study (Fig. 15), the required load to activate the slip system decreases, leading to the texture softening effect. This would lead to a drop in yield stress and lowering the flow stress of the material in general, as seen for the cases of alloys processed by ECAP compared to those treated by SSE (Figs. 13 and 14). Developments of sharp peaks at high SF values in the Schmid factor histograms of the ECAP-processed conditions (Fig. 15b, d and f), is in excellent accordance with the inclined arrangement of basal planes about ∼ 45° relative to the loading direction. The texture softening effect and decline of yield stress has been reported for different Mg alloys after being processed via ECAP [56,57], in which the basal planes were rearranged to a similar inclined configuration to the loading direction of mechanical testing.

Even though the ECAP-processed conditions exhibited lower yield stress and compressive strength, greater fracture strain values were reported for them after the same passes of processing compared to their counterparts processed by SSE (Figs. 13 and 14). This higher ductility can be again attributed to the easy orientation of basal planes providing a facilitated slip during plastic flow, which has also been mentioned for other Mg alloys processed via ECAP in the literature [58,59]. However, in either case of SSE or ECAP, the fracture strain declined continuously by raising the pass numbers. This behavior can be originated from the noticeable presence of $Mg_5(Gd,X)$ nano-particles and the increase in their volume fraction as the DRX proceeds by further straining during SPD processes. The $Mg_5(Gd,X)$ nano-particles would play a significant role in acting as potential sites for stress concentration and void nucleation during straining in the compression tests, leading to diminishing the ductility eventually [60]. The detrimental effect of dynamically precipitated nano-particles on the ductility of Mg alloys after being processed by SPD techniques were reported in previous works as well [61].

5. Conclusions

An extruded Mg−6Gd−3Y−1.5Ag (wt%) alloy was processed via two different severe plastic deformation (SPD) techniques of simple shear extrusion (SSE) and equal channel angular pressing (ECAP) at 553 K for different passes of 1, 2, 4 and 6. Microstructural and textural evolutions as well as mechanical properties of the alloys processed by both SSE and ECAP were compared and the following conclusions were drawn.

(1) EBSD results demonstrated that by progressive straining, the fraction of recrystallization and high angle grain boundaries (HAGBs) increased continuously and an average recrystallized grains size of about 1.3 μm was

achieved after 6 passes of processing for both techniques. The continuous decrease in the density of low angle grain boundaries (LAGBs), as deformation increased, was interpreted as the consequence of discontinuous dynamic recrystallization (DDRX) progressively growing from the grain boundaries to the grain interior.

(2) EBSD studies showed significant differences in the fraction of recrystallization and also density of HAGBs between SSE and ECAP-processed alloys, these being more pronounced in the early stages of straining. After the same number of passes, the samples processed by ECAP possessed greater fractions of fine recrystallized grains and also HAGBs compared to the ones processed by SSE, implying that DRX has proceeded with an accelerated rate for the case of ECAP. The enhanced DRX rate in ECAP was attributed to the greater equivalent strain rate in this technique.

(3) The study of crystallographic texture after processing via SSE and ECAP showed that after 4 and 6 passes of both SSE and ECAP the basal planes were arranged parallel to the shear planes. In the case of SSE, the basal planes were aligned parallel to extrusion direction (ED) with their poles along the normal direction (ND) and transverse direction (TD), while the basal planes for the ones treated by ECAP were inclined about 45° relative to ED. The observed difference in the texture components was attributed to the different strain paths and the geometrical position of shear planes relative to the main axes in both SSE and ECAP.

(4) As the number of passes increased the compressive yield stress and ultimate compressive strength of the alloys processed by both SSE and ECAP was raised continuously compared to the extruded alloy. The improvement in the mechanical properties of the SPD-processed alloys was attributed to the strengthening mechanisms of Hall-Petch and also Orowan hardening regarding the presence of dynamically precipitated $Mg_5(Gd,X)$ nanoparticles. However, after identical numbers of passes, the lower yield stress values recorded for the alloys processed by ECAP was related to the soft orientation of basal planes.

Declaration competing interest

The authors declare that they have no known competing financial interests or personal relationships that could have appeared to influence the work reported in this paper.

Funding

This research did not receive any specific grant from funding agencies in the public, commercial, or not-for-profit sectors.

References

[1] B.L. Mordike, T. Ebert, Mater. Sci. Eng. A 302 (2001) 37–45, doi:10.1016/S0921-5093(00)01351-4.
[2] M.K. Kulekci, Int. J. Adv. Manuf. Technol. 39 (2008) 851–865, doi:10.1007/s00170-007-1279-2.
[3] T. Al-Samman, Acta Mater. 57 (2009) 2229–2242, doi:10.1016/j.actamat.2009.01.031.
[4] X. Li, T. Al-Samman, S. Mu, G. Gottstein, Mater. Sci. Eng. A 528 (2011) 7915–7925, doi:10.1016/j.msea.2011.07.010.
[5] I. Basu, T. Al-Samman, G. Gottstein, Mater. Sci. Eng. A 579 (2013) 50–56, doi:10.1016/j.msea.2013.04.076.
[6] T. Al-Samman, G. Gottstein, Mater. Sci. Eng. A 490 (2008) 411–420, doi:10.1016/j.msea.2008.02.004.
[7] K. Edalati, A. Yamamoto, Z. Horita, T. Ishihara, Scr. Mater. 64 (2011) 880–883, doi:10.1016/j.scriptamat.2011.01.023.
[8] J.A. del Valle, P. Rey, D. Gesto, D. Verdera, J.A. Jiménez, O.A. Ruano, Mater. Sci. Eng. A. 628 (2015) 198–206, doi:10.1016/j.msea.2015.01.030.
[9] N. Azizi, R. Mahmudi, Mater. Sci. Eng. A 817 (2021) 141385, doi:10.1016/j.msea.2021.141385.
[10] X. Luo, Z. Feng, T. Yu, T. Huang, R. Li, G. Wu, N. Hansen, X. Huang, Mater. Sci. Eng. A 772 (2020) 138763, doi:10.1016/j.msea.2019.138763.
[11] Q. Wang, Y. Mu, J. Lin, L. Zhang, H.J. Roven, Mater. Sci. Eng. A 699 (2017) 26–30, doi:10.1016/j.msea.2017.05.080.
[12] M. Al-Maharbi, I. Karaman, I.J. Beyerlein, D. Foley, K.T. Hartwig, L.J. Kecskes, S.N. Mathaudhu, Mater. Sci. Eng. A 528 (2011) 7616–7627, doi:10.1016/j.msea.2011.06.043.
[13] M.M. Hoseini-Athar, R. Mahmudi, R. Prasath Babu, P. Hedström, Scr. Mater. 186 (2020) 253–258, doi:10.1016/j.scriptamat.2020.05.042.
[14] R.Z. Valiev, T.G. Langdon, Prog. Mater. Sci. 51 (2006) 881–981, doi:10.1016/j.pmatsci.2006.02.003.
[15] Y. Fu, J. Sun, Z. Yang, B. Xu, J. Han, Y. Chen, J. Jiang, A. Ma, Mater. Charact. 165 (2020) 110398, doi:10.1016/j.matchar.2020.110398.
[16] B. Li, B. Teng, G. Chen, Mater. Sci. Eng. A 744 (2019) 396–405, doi:10.1016/j.msea.2018.12.024.
[17] R.B. Figueiredo, T.G. Langdon, J. Mater. Sci. 45 (2010) 4827–4836, doi:10.1007/s10853-010-4589-y.
[18] M. Janeček, S. Yi, R. Král, J. Vrátná, K.U. Kainer, J. Mater. Sci. 45 (2010) 4665–4671, doi:10.1007/s10853-010-4675-1.
[19] P. Minárik, R. Král, J. Pešička, S. Daniš, M. Janeček, Mater. Charact. 112 (2016) 1–10, doi:10.1016/j.matchar.2015.12.002.
[20] P. Minárik, J. Veselý, R. Král, J. Bohlen, J. Kubásek, M. Janeček, J. Stráská, Mater. Sci. Eng. A 708 (2017) 193–198, doi:10.1016/j.msea.2017.09.106.
[21] F. Kang, J.T. Wang, Y. Peng, Mater. Sci. Eng. A 487 (2008) 68–73, doi:10.1016/j.msea.2007.09.063.
[22] N. Pardis, R. Ebrahimi, Mater. Sci. Eng. A 527 (2009) 355–360, doi:10.1016/j.msea.2009.08.051.
[23] N. Bayat Tork, N. Pardis, R. Ebrahimi, Mater. Sci. Eng. A 560 (2013) 34–39, doi:10.1016/j.msea.2012.08.085.
[24] N. Pardis, R. Ebrahimi, Mater. Sci. Eng. A 527 (2010) 6153–6156, doi:10.1016/j.msea.2010.06.028.
[25] A. Rezaei, R. Mahmudi, C. Cayron, R. Loge, Mater. Sci. Eng. A 806 (2021) 140803, doi:10.1016/j.msea.2021.140803.
[26] F. Bachmann, R. Hielscher, H. Schaeben, Solid State Phenom. 160 (2010) 63–68, doi:10.4028/www.scientific.net/SSP.160.63.
[27] W. Pantleon, Scr. Mater. 58 (2008) 994–997, doi:10.1016/j.scriptamat.2008.01.050.
[28] A. Rezaei, R. Mahmudi, C. Cayron, R.E. Loge, Mater. Sci. Eng. A 802 (2021) 140616, doi:10.1016/j.msea.2020.140616.
[29] A. Rezaei, R. Mahmudi, R. Loge, Metall. Mater. Trans. A 51 (2020) 5139–5153, doi:10.1007/s11661-020-05937-4.
[30] A. Movahedi-Rad, R. Mahmudi, Mater. Sci. Eng. A. 614 (2014) 62–66, doi:10.1016/j.msea.2014.07.022.
[31] D.F. Gatz, L. Smith, Atmos. Environ. 29 (1995) 1185–1193, doi:10.1016/1352-2310(94)00210-C.
[32] A. Galiyev, R. Kaibyshev, G. Gottstein, Acta Mater. 49 (2001) 1199–1207, doi:10.1016/S1359-6454(01)00020-9.
[33] F.J. Humphreys, M. Hatherly, Recrystallization and Related Annealing Phenomena, 2nd edition, Elsevier, Oxford, 2004.

[34] S. Yu, C. Liu, Y. Gao, S. Jiang, Z. Bao, Mater. Charact. 131 (2017) 135–139, doi:10.1016/j.matchar.2017.07.015.
[35] T. Sakai, A. Belyakov, R. Kaibyshev, H. Miura, J.J. Jonas, Prog. Mater. Sci. 60 (2014) 130–207, doi:10.1016/j.pmatsci.2013.09.002.
[36] J. Zhang, B. Chen, C. Liu, Mater. Sci. Eng. A 612 (2014) 253–266, doi:10.1016/j.msea.2014.06.058.
[37] D.K. Sun, C.P. Chang, P.W. Kao, Metall. Mater. Trans. A 41 (2010) 1864–1870, doi:10.1007/s11661-010-0220-8.
[38] A.G. Beer, M.R. Barnett, Metall. Mater. Trans. A 38 (2007) 1856–1867, doi:10.1007/s11661-007-9207-5.
[39] B. Wang, C. Liu, Y. Gao, S. Jiang, Z. Chen, Z. Luo, Mater. Sci. Eng. A 702 (2017) 22–28, doi:10.1016/j.msea.2017.06.038.
[40] H. Xiao, B. Tang, C. Liu, Y. Gao, S. Yu, S. Jiang, Mater. Sci. Eng. A 645 (2015) 241–247, doi:10.1016/j.msea.2015.08.022.
[41] Q. Zhang, Q. Li, X. Chen, J. Zhao, J. Bao, Z. Chen, J. Mater. Res. Technol. 15 (2021) 37–51, doi:10.1016/j.jmrt.2021.08.013.
[42] E. Bagherpour, F. Qods, R. Ebrahimi, IOP Conf. Ser. Mater. Sci. Eng. 63 (2014) 012046, doi:10.1088/1757-899X/63/1/012046.
[43] F. Liu, Y. Liu, J.T. Wang, Mater. Sci. Forum. 850 (2016) 419–425, doi:10.4028/www.scientific.net/MSF.850.419.
[44] A. Gilbert, B.A. Wilcox, G.T. Hahn, Philos. Mag. J. Theor. Exp. Appl. Phys. 12 (1965) 649–653, doi:10.1080/14786436508218904.
[45] H. Jiang, J. Dong, M. Zhang, Z. Yao, Metall. Mater. Trans. A 47 (2016) 5071–5087.
[46] S. Mandal, M. Jayalakshmi, A.K. Bhaduri, V.S. Sarma, Metall. Mater. Trans. A 45 (2014) 5645–5656, doi:10.1007/s11661-014-2480-1.
[47] H. Zhang, K. Zhang, H. Zhou, Z. Lu, C. Zhao, X. Yang, Mater. Des. 80 (2015) 51–62, doi:10.1016/j.matdes.2015.05.004.
[48] F. Sayari, R. Roumina, R. Mahmudi, M.M. Hoseini-athar, P. Hedström, J. Alloys Compd. 908 (2022) 164407, doi:10.1016/j.jallcom.2022.164407.
[49] N. Bayat Tork, H. Saghafian, S.H. Razavi, K.J. Al-Fadhalah, R. Ebrahimi, R. Mahmudi, J. Mater. Res. Technol. 8 (2019) 1288–1299, doi:10.1016/j.jmrt.2018.06.023.
[50] S.R. Agnew, P. Mehrotra, T.M. Lillo, G.M. Stoica, P.K. Liaw, Mater. Sci. Eng. A 408 (2005) 72–78, doi:10.1016/j.msea.2005.07.052.
[51] M.M. Hoseini-Athar, R. Mahmudi, R.P. Babu, P. Hedström, Mater. Sci. Eng. A 808 (2021) 140921, doi:10.1016/j.msea.2021.140921.
[52] M. Sabbaghian, R. Mahmudi, K.S. Shin, Mater. Sci. Eng. A 845 (2022) 143218, doi:10.1016/j.msea.2022.143218.
[53] Y.H. Wang, J.M. Kang, Y. Peng, T.S. Wang, N. Hansen, X. Huang, Scr. Mater. 155 (2018) 41–45, doi:10.1016/j.scriptamat.2018.06.019.
[54] H. Pan, G. Qin, Y. Huang, Y. Ren, X. Sha, X. Han, Z.Q. Liu, C. Li, X. Wu, H. Chen, C. He, L. Chai, Y. Wang, J. Nie, Acta Mater. 149 (2018) 350–363, doi:10.1016/j.actamat.2018.03.002.
[55] W.J. Kim, C.W. An, Y.S. Kim, S.I. Hong, Scr. Mater. 47 (2002) 39–44, doi:10.1016/S1359-6462(02)00094-5.
[56] W.J. Kim, S.I. Hong, Y.S. Kim, S.H. Min, H.T. Jeong, J.D. Lee, Acta Mater. 51 (2003) 3293–3307, doi:10.1016/S1359-6454(03)00161-7.
[57] T. Krajňák, P. Minárik, J. Gubicza, K. Máthis, R. Kužel, M. Janeček, Mater. Charact. 123 (2017) 282–293, doi:10.1016/j.matchar.2016.11.044.
[58] S.R. Agnew, J.A. Horton, T.M. Lillo, D.W. Brown, Scr. Mater. 50 (2004) 377–381, doi:10.1016/j.scriptamat.2003.10.006.
[59] T. Liu, Y.D. Wang, S.D. Wu, R.Lin Peng, C.X. Huang, C.B. Jiang, S.X. Li, Scr. Mater. 51 (2004) 1057–1061, doi:10.1016/j.scriptamat.2004.08.007.
[60] E. Dogan, S. Wang, M.W. Vaughan, I. Karaman, Acta Mater. 116 (2016) 1–13, doi:10.1016/j.actamat.2016.06.011.
[61] J. Li, J. Liu, Z. Cui, Mater. Sci. Eng. A 643 (2015) 32–36, doi:10.1016/j.msea.2015.07.028.